Alma Mater Studiorum · Università di Bologna

Scuola di Scienze
Dipartimento di Fisica e Astronomia
Corso Magistrale in Fisica del sistema terra

A comparison between vertical mixing parameterizations in the Levantine Sea

Relatore:
Prof. Nadia Pinardi

Correlatore
Dott. Francesco Trotta

Presentata da:
Enrico Moresco

Anno Accademico 2021/2022

Contents

Chapter 1

Introduction

The closure problem of Reynolds Average Navier Stokes equations has been faced up in several ways over time and in its application to geophysical mixing a multitude of solutions are possible. While great strides have been made in understanding turbulence processes since the days of A. Kolmogoroff, Ludwig Prandtl, and G.I. Taylor, there is still much controversy about the modelling of turbulent mixing in both the laboratory and nature. Turbulence modelers, however, take the view that practical applications cannot wait for a complete understanding of turbulence and the outcome of the applications of a turbulence model provides the necessary justification (or lack of it) for the simplifications that are inevitable in deriving a practical turbulence model. Both of these schools of thought have been and still are essential to progress in the application of our knowledge on turbulence to the solution of practical problems in geophysics. Initially, turbulence researchers had only observational data in the laboratory for creating and testing their intuitions about turbulent mixing. Newer techniques like direct numerical simulations (DNS), large eddy simulations (LES) and renormalization group analysis (RNG) allow us to investigate previously unattainable aspects of turbulent mixing. There is also a huge increasing availability of data from atmospheric and oceanic, as well as laboratory, mixed layers that allow us to test the validity of a model in practical situations. Since most mixing models will perform acceptably only in simple mixed and boundary layers, or just in definite, unflexible conditions, considerable effort and thought are invested to make a model "universally" applicable, especially to complex turbulence that involves additional strain rates. In the geophysical context, the need to construct accurate and reliable models of mixing in the oceanic and atmospheric mixed layers has become increasingly important and urgent. Mixed layers (ML) play an important role in air-sea interactions on a wide variety of temporal and spatial scales, and are a key element to our understanding of processes such as E1 Ninho - Southern Oscillation (ENSO) and carbon-dioxide induced global warming, and thus to climatic fluctuations on both short and long time scales (Smith, 1993). Mixed layers also determine the dispersal of pollutants in the upper ocean. The evolution of the mixed layer is essentially driven by two factors, as seen in Figure 1.1 in a simplified one-dimensional model, the downward diffusion that increases the thermocline depth the upward advection that decreases it (Talley et al., 2011), the equilibrium between two processes determines the mixed layer depth and it's evolution. Despite the im-

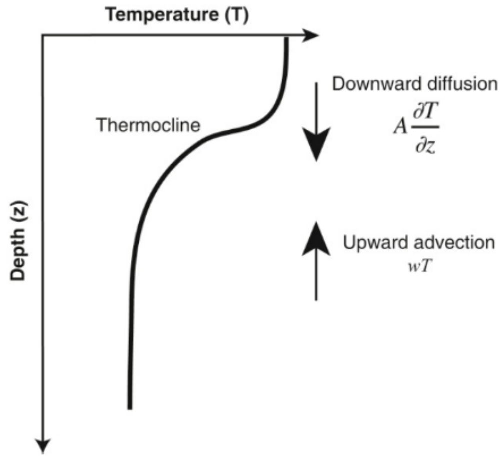

Figure 1.1: Vertical processes that can maintain the thermocline in a simplified one-dimensional model. (Talley et al., 2011)

portance of the ML description , the parameterization of the turbulent mixing in thin ocean surface boundary layers (OSBL), which occupy the upper 100 m or so of the ocean, lead to systematic and substantial errors in the depth of the OSBL in global climate models, which then leads to biases in sea surface temperature. As (Belcher, 2012) argue one reason is that current parameterizations are missing key surface-wave processes that force Langmuir turbulence that deepens the OSBL more rapidly than steady wind forcing. In general the choice of the vertical mixing parameterization has a key role in the modeling of the ocean surface boundary layer and the investigation of the effects of different turbulent submodels in different case of studies is imperative to get the general overview and then be able to improve the current modelizations.

1.0.1 Thesis objectives

Since the analysis and forecast data, commonly used from CMCC and provided by CMEMS, as the default NEMO set up, use both a Richardson dependent closure scheme (Pacanowski and Philander, 1981), and since this widely and commonly used closure does not describe the aforementioned Langmuir turbulence, would be interesting to compare the behavior of the same ocean model but implemented by different turbulent closures. To prepare this comparison, two important choices are to be made: the choose of the alternative turbulent closures and the choose of the case of study.

As far as concerns the turbulent closures, in the studies about the Langmuir turbulence, the Generic Length Scale closure scheme is widely used, above all: (Kantha and Clayson, 1994) uses a Mellor Yamada model, Lars uses a k-ϵ closure) Mellor, G. and (Mellor and Blumberg, 2004) also proposes a k-ϵ closure) mainly for it's flexibility and the superior descriptive capability given from a two-equation-closure.

Also a more simple model based on a prognostic equation for TKE, the turbulent kinetic energy, and a closure assumption for the turbulent length scales is interesting to observe. This turbulent closure model has been developed by (Bougeault and Lacarrere, 1989) in the atmospheric case, adapted by (Gaspar et al., 1990) for the oceanic case, and embedded in OPA, the ancestor of NEMO, by (Blanke and Delécluse, 1993) for equatorial Atlantic simulations. Since then, significant modifications have been introduced by (Madec et al., 1998) in both the implementation and the formulation of the mixing length scale. The interesting part is that also in this 1-equation simple model had been uploaded a Langimour correction term, following (Mellor and Blumberg, 2004). Could be interesting to observe if a less resource requiring submodel as TKE-closure scheme can or cannot reach the same quality of the GLS-closure scheme.

About the case of study, since similar confronts has already been done in the atlantic, above all: (Ali et al., 2019).

Could be more enriching to move in a different oceanic situation, like a warmer, more saline, shallower sea as the Mediterranean; in addition to that evidences of a discrepancy between ocean model results and experimental data occurred in an high circulation characterized case (Gunduz et al., 2013).
Furthermore we should consider that a situation of intense circulation is a really interesting test for the turbulent models: a circulating system is usually more energetic, shows a more intense shear stress and is less interacting with their boundaries, for this reason the consequent differences in the forecasting of the Mixed Layer Depth between several models should be more visible. So, fist of all is important to analyze the circulation of the Mediterranean Sea to look for the most promising case of study.

1.1 Mediterranean General circulation

Currents systems	Components
System 1	1a: Atlantic Water Current 1b: Western and Eastern Alboran Gyres 1c: Almera-Oran front 1d: Almera-Oran cyclonic eddy 1e: Algerian Current segments 1f: Western Mid-Mediterranean Current 1g: Southern Sardinia Current
System 2	2a: Gulf of Lyon Gyre 2b: Liguro-Provencal-Catalan Current 2c: Western Corsica Current
System 3	3a: South-Western Tyrrhenian Gyre 3b: South-Eastern Tyrrhenian Gyre 3c: Northern Tyrrhenian Gyre 3d: Middle Tyrrhenian Current 3e: Eastern Corsica Current
System 4	4a: Atlantic-Ionian Stream 4b: Sicily Strait Tunisian Current 4c: Syrte Gyre 4d: Eastern Ionian Current 4e: Pelops Gyre 4f: Northern IonianCyclonic Gyre
System 5	5a: Eastern South-Adriatic Current 5b: Middle Adriatic Gyre 5c: South Adriatic Gyre 5d: Western Adriatic Coastal Current
System 6	6a: Cretan Passage Southern Current 6b: Mid-Mediterranean Jet 6c: Southern Levantine Current 6d: Mersa Matruh Gyre System 6e: Rhodes Gyre 6f: Shikmona Gyre System 6g: Asia Minor Current 6h: Ierapetra Gyre 6i: Western Cretan Cyclonic Gyre
System 7	7a: Cretan Sea Westward Current 7b: Southward Cyclades Current 7c: North Aegean Anticyclone

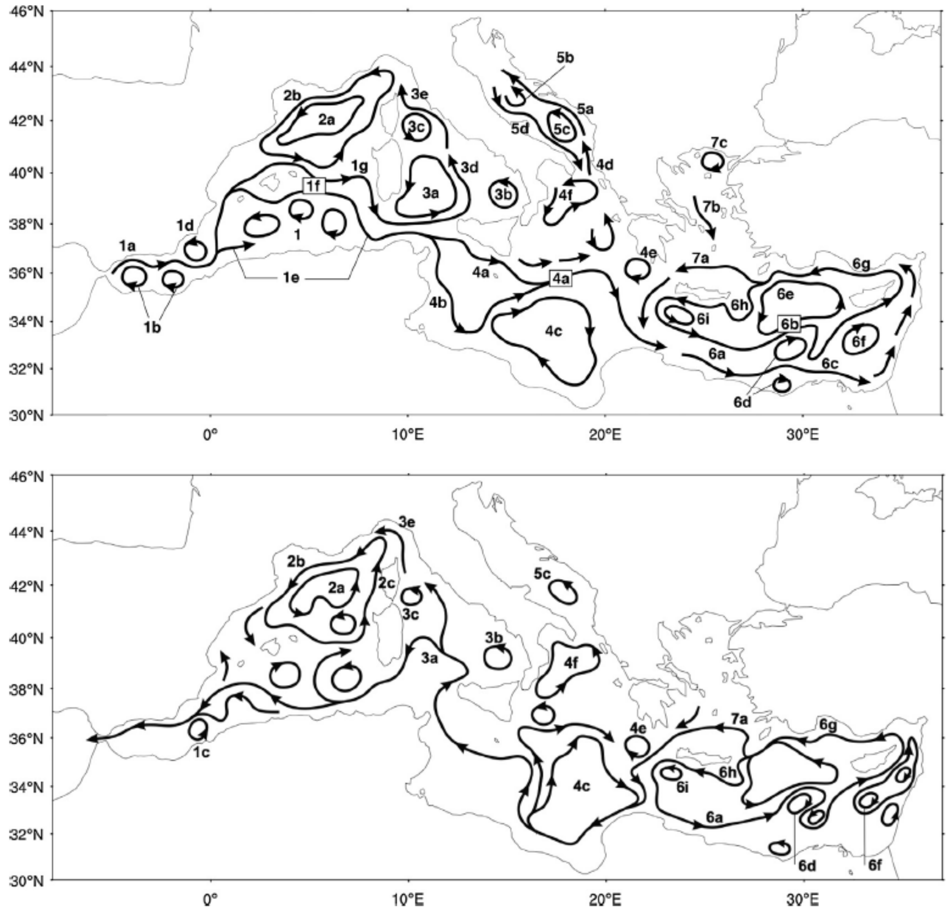

Figure 1.2: Representation of the mean surface circulation structures from the mean flow field for the period 1987-2007 reanalysis. Top Figure: surface circulation. Bottom Figure: 200-300 m average circulation. Reproduced from (Pinardi and Masetti, 2000)

The Mediterranean Sea is governed by a large scale circulation both in the horizontal and vertical directions, and it is driven by three major forcings interacting with each other (N. Pinardi and Navarra, 1993):

- the thermal and evaporative fluxes at the air-sea interface (between seasonal and decadal);
- the inflow-outflow transport at Gibraltar Strait;
- the wind stress.

The first drive the overturning circulation and control water mass formation processes with variable timescales, the second one is the mechanism controlling the overall basin water budget on decadal timescales and the latter, with a strong seasonal varibility,

forces the circulation at sub-basin spatial scale.
Thermal and wind effects often act on the same spatial scales, the former inducing water transformation processes and the latter causing the spreading of the newlyformed water mass (N. Pinardi and Navarra, 1993).

Four different core masses were individuated and described by (Wüst, 1961) analyzing the spreading and mixing of vertical processes:

- the near-surface water, between 0 and 75 m depth,
- the intermediate water, between 200 and 600 m,
- the deep water, between 1500 and 3000 m
- the bottom water, at depths to 4200 m.

A critical discriminant between the deep waters and the upper ones is the Strait of Sicily orography: since the Strait of Sicily is only 300 m deep, down to this depth the Mediterranean circulation spreads over the entire basin, while deep motion is limited within the sub-basin where is has been forced. (Nadia Pinardi, 2015) proposed an exhaustive description of the Mediterranean dynamical pattern at the surface and between 200-300 m depth, shown on Figure 1.1, analyzing the horizontal circulation structures; this superior description states that time-mean circulation in the Mediterranean Sea is made up of both boundary and open ocean intensified jets at the border of cyclonic and anticyclonic gyres.

The basin circulation shows a double gyre structure due to the wind stress sign, positive in the nothern areas characterized by cyclonic circulations and negative in the southerns, often showing an anticyclonic motion. Moreover the formation processes of intermediate and deep water contribute, as also happens in the North Atlantic ocean, to force the cyclonic northern gyres, while the southern gyres involve intermediate-mode waters which compose the permanent thermocline of the basin.

Hereafter we start describing the main water masses paths in the surface and intermediate layers, providing a preliminar characterization of the phenomenon and its origins. The Atlantic Water Current characterizes the surface mean flow in the Mediterranean Sea, spreading eastward along the African coast as is modified by air-sea interactions. As a result, it becomes Modified Atlantic Water (MAW) which usually occupies the upper 100 m layer and is characterized by a higher salinity (38- 38.3 psu) than Gibraltar inflow waters due to evaporation and mixing (Demirov and Pinardi, 2007). Numerical model simulations (Speich et al., 1996) and laboratory experiments (Gleizon et al., 1996) have demonstrated a conjunction of the Gibraltar Strait regime, the general pattern of the Atlantic Flow in the Alboran Sea, and the circulation of the underlying Mediterranean water. On the other hand, intermediate waters are mainly Levantine Intermediate Water, which originates in the Levantine basin but can be found all around the Mediterranean Sea. In Figure 1.2 is represented its large-scale distribution described in (Pinardi and Masetti, 2000); even though the main pattern moves westward and northward, several branchings currents spread LIW all around the basin. The principal paths bring the LIW to the Gulf of Lyon and to the northern Adriatic Sea, where it generates deep convection events, hence producing deep water formation processes.

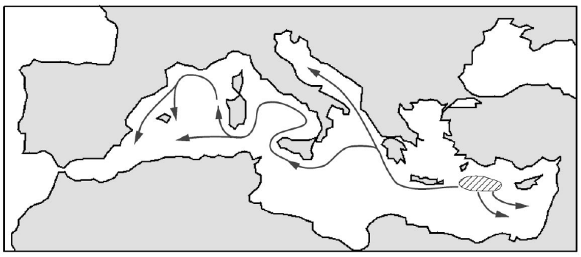

Figure 1.3: LIW dispersal pathways as synthetised from recent modeling and observational studies. Reproduced from (Pinardi and Masetti, 2000)

1.1.1 Levantine Sea

The Levantine is the Mediterranean portion comprehended between the Aegean Sea in the northwest, Turkey in the north and north-east, Syria, Lebanon, Israel and the Gaza Strip in the east and Egypt in the south.

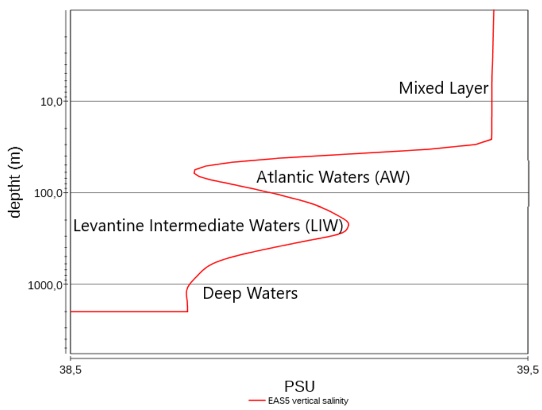

Figure 1.4: Levantine waters schematic on EAS5 reanalysis data, vertical salinity plot, daily mean day 5/10/2020.

Its western border is amorphous since in terms of oceanography it depends by the variability of the currents (in particular of the Mid-Mediterranean Jet) and, with them, of the general circulation. The open western border to the next part of the Mediterranean (the Libyan Sea) is generally defined as a line from headland Ras al-Helal in Libya to Gavdos, south of the western half of Crete. As the all Mediterranean, Levantine Sea is a concentration basin since evaporation exceeds precipitation and runoff (Carter, 1956). The termohaline circulation of the basin have been described by (Wüst, 1961), and the water masses have been characterized by (Lacombe et al., 1985). They consist of three distinct water mass layers:

- a layer of Atlantic Water (AW) between the surface and approximately 100 m entering from the Strait of Gibtair and characterized by low temperatures (about 15°C) and low salinity (about 38.5 PSU)
- a layer of Intermediate Levantine Water (LIW) between 200 and 600 m that corresponds to a subsurface salinity maximum (>>38.5 PSU) and is formed in the eastern Levantine basin
- the deep waters down to the bottom.

Since only Atlantic Waters and Levantine Intermediate Waters are exchanged between eastern and western basins because of the swallow sill at the strait of Sicily, the deep waters of the Eastern and Western basins are formed separately: in the Adriatic for the eastern basin and in the Northern Balearic basin for the western one (Stommel, 1972). Since the Mid-Mediterranean Jet form a meandering current along the Libyan coast and progress up to the Levantine basin, the local currents are generally cyclonic , forming gyres in the Ionian Sea and southeast of Rhodes, in contrast with the general distribution of vorticity described in the previous section. The flow has characteristic velocities of 1-10 cm/s. At 500 m the current continue to be generally cyclonic, but the flow appears to be more distorted by the topography of the basin, breaking up into smaller gyres.

The thermohaline circulation of the eastern Levantine basin is of particular interest becouse of the importance of intermediate and deep water formation processes. The Levantine Basin is characterised with the highest salinity at the surface (39-39,5 psu) and intermediate layers of the Mediterranean, less saline waters of Atlantic origin spread at the sub-surface layers, almost throughout the basin, as a results of the water volume compensation for the high rates of the sea water evaporation in the Levantine and of the outflow of the intermediate water into the North Atlantic, this gives the Levantine water unique salinity and temperature vertical profiles shown if Fig. 1.4

The Rhoder gyre the Eagean Sea (Oszoy et al. 1981) and the region offshore of Egypt were individuated as regions of LIW formation processes, but no clear definition of the kinematics and dynamics of such events or of subsequent water spreading mechanisms is available.

1.2 The Mediterranean circulation variability

(Nadia Pinardi, 2015) observed that Mediterranean circulation time variability peaks at the seasonal and interannual time scales, as indicated by experimenatal observations (Larnicol et al., 2002); (Poulain et al., 2012) and numerical simulations (Demirov and Pinardi, 2002);(Molcard et al., 2002). Hovever this behaviour isn't uniform on the basin, as (Fusco et al., 2003) stated: the temporal and spatial variability of temperature profiles are significantly different in the Western and Eastern Mediterranean.

In the Western Mediterranean and in the Adriatic Sea, the winter cooling leads to a loss of thermal stratification. In the Eastern Mediterranean the stratification is always observed, although varying with the seasons and strongly influenced by long-lasting gyres.

1.2.1 Seasonal variability

According to (Pinardi and Masetti, 2000) the seasonal variability can be strictly related to changes in heat and momentum fluxes, as it involves mainly:

- the winter geographical location of deep and intermediate convection sites (Leaman and Schott, 2003); (Artegiani, 1997),
- the surface water mass formation cycle (Hecht et al., 1988)
- the seasonal reversal of currents in different portions of the basin (Tziperman and Malanotte-Rizzoli, 1991),
- the strength of mesoscale flow fields (Ayoub et al., 1998).

Both superficial water masses properties and large scale circulation are strongly related to the seasonal oscillations of the external forcing (wind forcing, heat and salinity fluxes, buoyancy, fresh water, etc). Moreover the seasonal structure of the circulation and the water masses properties can be connected to the space and time arrangements of the meteorological forcing over the basin.

The surface atmospheric flow field is characterized by two subregional wind regimes:

- winter Westerlies winds interact with the local orography,
- in summer there is a strong land-sea temperature contrast.

This winter wind pattern is among the main causes of the already mentioned characteristic vorticity distribution in the mediterranean, with cyclonic circulation in the north and anticyclonic circulation in the southern zones. Nevertheless, since the topography and the viscous boundary effects contribute to the potential vorticity balance as well (N. Pinardi and Navarra, 1993), the vorticity distribution often diverges from the previous description, expecially in the southern areas. Figure 1.3 shows a schematic of the wind-driven circulation in wintertime, simplifying the patterns of Figure 1.1.

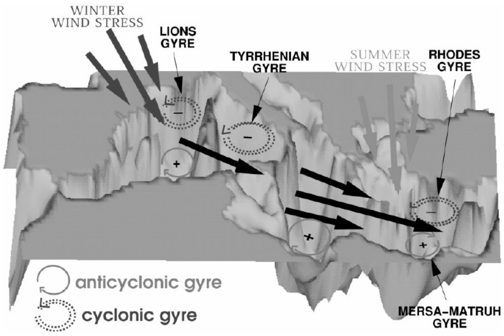

Figure 1.5: Schematic of the wind-driven circulation in wintertime conditions. The thick arrows indicate the direction of winter surface wind stress field. Sverdrup-induced wind-driven gyres are drawn, consistently with vorticity input from the two jets sides. Reproduced from (Pinardi and Masetti, 2000)

1.2.2 Interannual variability

The interannual variability of the basin can be analysed by investigating the main circulation patterns and the changes at 30 m depth, approximately at the bottom of the Ekman layer. The intermediate variability is punctuated by events mainly forced by winter atmospheric anomalies strong enough to shift the timing of the seasonal cycle(Korres et al., 2000).

The largest changes happen in the Eastern Mediterranean, where the Northern Ionian Reversal phenomenon (NIR) has occurred as the largest decadal variability event in the past 20 years (Nadia Pinardi, 2015). The atmospheric momentum and heat fluxes, as well as wind stress variance are found to be the main driving forces of interannual timescale circulation variability, which is larger in the Eastern than in the Western Mediterranean. Nevertheless interannual variability has a component which is related to the mesoscale field, too. In fact, various studies demonstrate that interannual variability aspects involve the following processes:

- large variations in volume transport between basins at the Straits (Astraldi et al., 1995),
- changes in the flow direction in several regions (Hecht et al., 1988); (Artale et al., 1994),
- intermediate and deep water mass formation rate (Nittis and Lascaratos, 1998),

- sudden switches in the deep water mass formation areas for the EMED (Roether and Manca, 1996)
- abrupt changes in LIW characteristics (A. Hecht, 1992).

Relative to the seasonal case, interannual variabilities are more difficult to explain since several mechanisms may contribute, e.g. meteorological anomalies with immediate or delayed effects, and internal nonlinear ocean dynamics which introduce chaotic elements into the redistribution of water masses.

Chapter 2

Modelling Framework

2.1 Limited area modeling with SURF

This section describes the limited area model used to create the set-ups for our oceanic forecasts, nested in the EAS5 product in the area of the Eastern Levantine Sea. We used the University of Bologna SURF model with the NEMO (3.6) code, to maintain the same physical equations as in the father model. The Structured and Unstructured grid Relocatable ocean platform for Forecasting (SURF) is an open-source package designed to generate high-resolution, nested model set-ups for oceanic forecasts over limited domains of interest. SURF requires coarser-resolution ocean forecasts for the initial and boundary conditions and atmospheric forcing to force the circulation. SURF-NEMO (Trotta et al., 2016); (Trotta et al., 2021) provides a numerical platform for forecasting hydrodynamic and thermodynamic fields at high spatial and temporal resolutions and is designed to be embedded in any region of a larger-scale ocean prediction system, at coarser-resolution. Furthermore it includes multiple nesting capabilities (i.e., consecutive nested models can be implemented with increasing grid resolutions), starting with the first nesting in a large-scale ocean model and reaching horizontal grid resolutions of a few hundred metres. For each nesting, the parent coarse-grid model provides the initial and lateral boundary conditions for the SURF child components.

2.1.1 Work-Flow

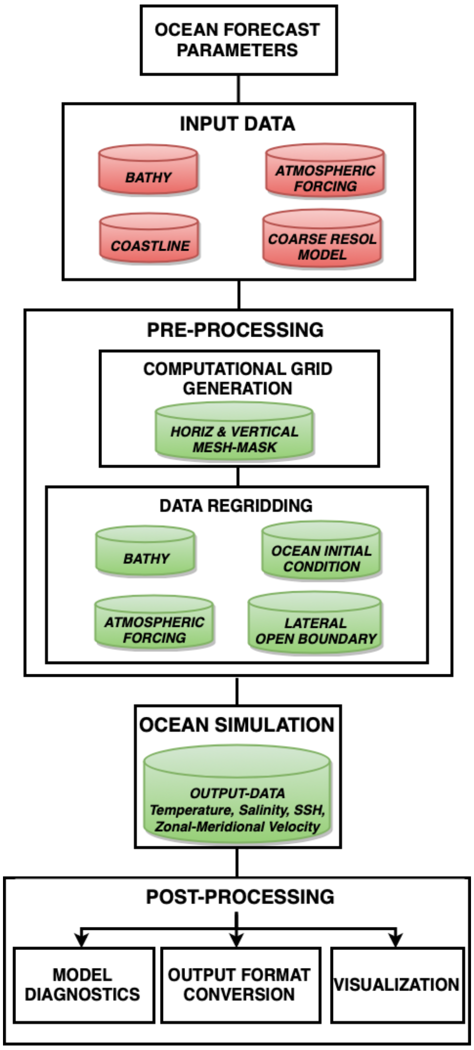

Figure 2.1

The schematic work-flow diagrams in Fig. 2.1 shown the steps involved in the SURF-NEMO numerical platform. The steps are grouped as follows:

- Initialization: the user specifies the values of the input simulation parameters for the ocean model in the configuration file (horizontal and vertical grids, subgrid scale parameterizations, etc.) for the specific experiment selected.

- Access and download of the input datasets: this is an automated step in which the input datasets for the selected simulation period are downloaded from remote or local data repositories, as specified in the configuration file. The input data are the bathymetry, the coastline, the atmospheric forcing and the coarse resolution parent ocean model for the initial and lateral boundary condition datasets.

- Spatial numerical grid generation: this is an automated step that generates the horizontal and vertical grid for the nested model.

- Input data regridding: this is an automated step that generates the bottom topography, surface forcing, initial and open lateral boundary conditions datasets on the child grid.

- Forecast: another automated step in which the NEMO code is exectuted to produce the final outputs.

- Post-processing: in this step the visualization and analysis procedures of the final outputs are considered. However this part wasn't utilized since several particular necessities for our case of study are not satisfied yet

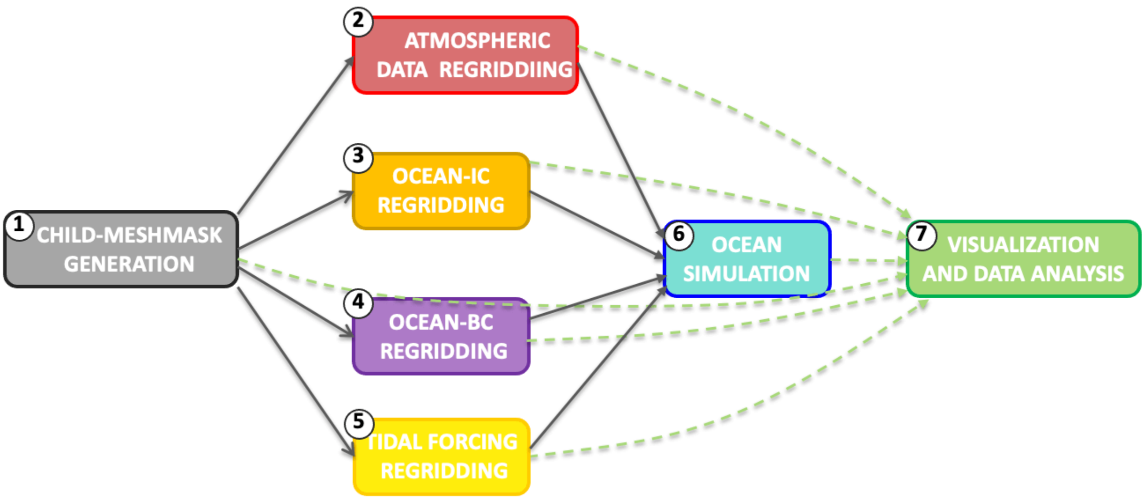

Figure 2.2: SURF workflo dependency schematic

The graphical calling function flow shown in Figure 2.2 represent all paths traversed through a program during its execution and shows how the program is completed from start to finish, step-by-step. The six macro-tasks identified are:

1) child meshmask generation;
2) atmospheric data regridding;
3) ocean IC data regridding;
4) ocean BC data regridding and OBC data extraction;
5) ocean model simulation; and
6) visualization and data analysis.

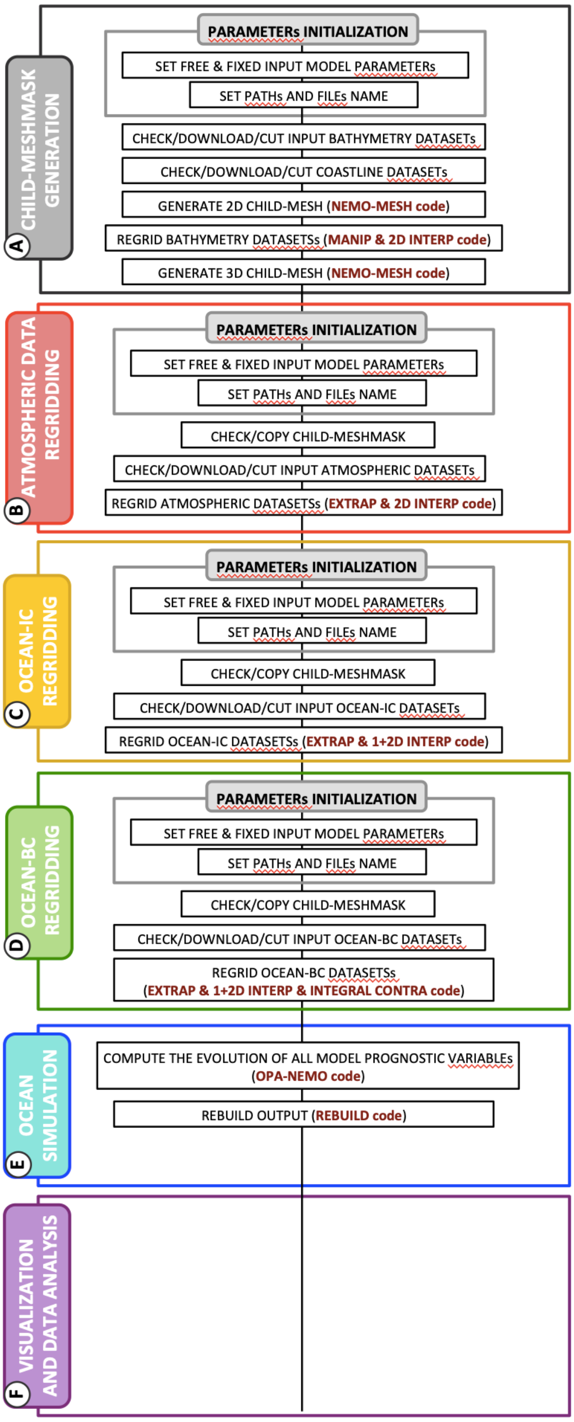

Figure 2.3: SURF sequential workflow

2.1.2 Horizontal grid

The horizontal grid generation is managed by the NEMO-MESH code. SURF uses a rectangular (or latitude-longitude)staggered grid in a spherical coordinate system λ, φ. The horizontal grid (expressed in degrees) is generated by specifying the number of points n_λ and n_φ,respectively, in zonal and meridional directions, and the respective grid sizes $\Delta\lambda$ and $\Delta\varphi$ (in degrees) and the longitude and latitude $(\lambda, \varphi)_{1,1}$ of the first row and first column of the T grid. On the $\lambda\varphi$ plane, the location of the T points of the grid are:

$$\begin{aligned} \lambda_{i,j} &= \lambda_{11} + (i-1)\Delta\lambda \quad \text{with } i = 1.....n_\lambda \\ \varphi_{i,j} &= \varphi_{11} + (j-1)\Delta\varphi \quad \text{with } j = 1.....n_\varphi \end{aligned} \tag{2.1}$$

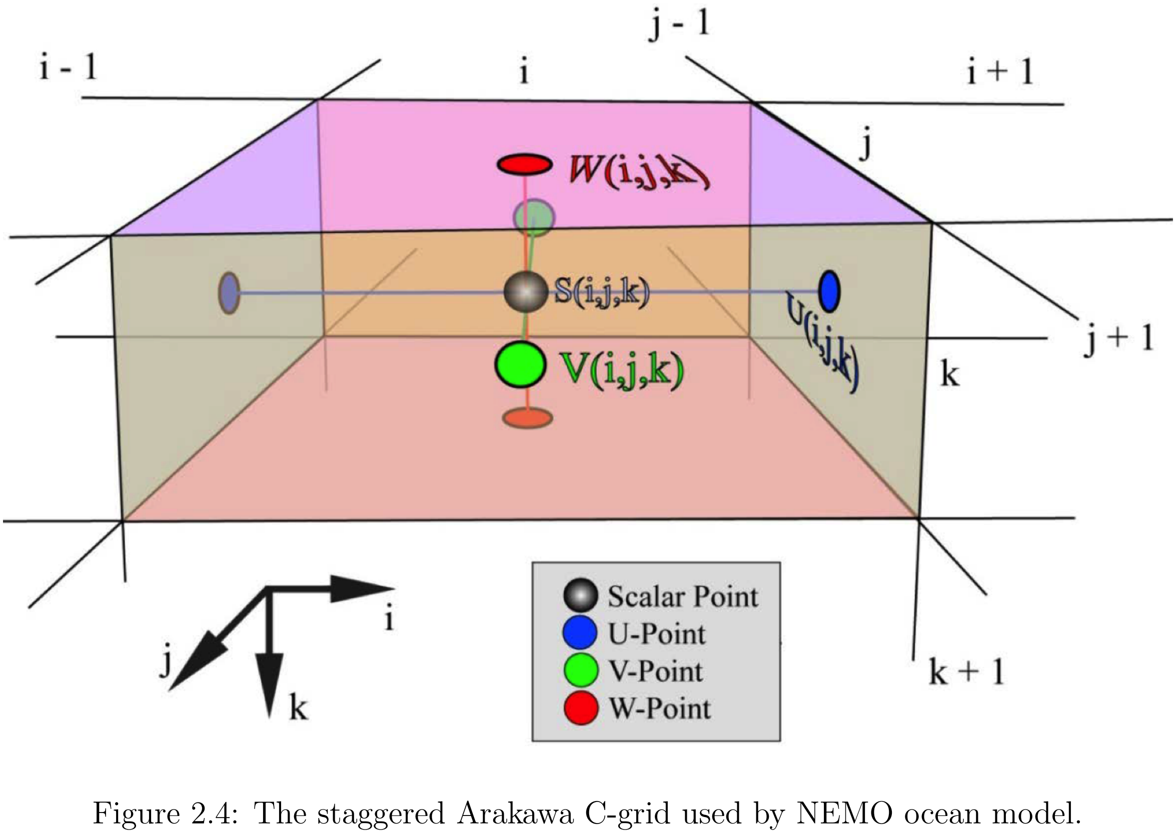

Figure 2.4: The staggered Arakawa C-grid used by NEMO ocean model.

The u, v points of the grid are shifted by half a grid width in the zonal e/o meridional direction, as indicated in Fig. 2.4

2.1.3 Vertical grid

The type of vertical grid used corresponds to geopotential z-coordinate levels with partial bottom cell representation of the bathymetry. After the bathymetry z $= H(\lambda, \varphi)$ and the number of levels $n_z$have been specified, the vertical location of w- and t-levels (expressed in metres) is managed in NEMO by a set of non-uniform z-coordinate levels, given by the definition of the following analytic expression:

$$z(k) = h_{sur} - h_0 k - h_1 log[cosh((k - h_{th})h_{cr})] \quad (2.2)$$

where the coefficients h_{sur}, h_0, h_1, h_{th} and h_{cr} are the parameters to be specified. h_{cr} represents the stretching factor of the grid and h_{th} is the approximate model level at which maximum stretching occurs. This expression enables stretched z-coordinate vertical levels to be defined, which are smoothly distributed along the water column, with appropriate thinning designed to better resolve the surface and intermediate layers.

2.1.4 Lateral Open Boundary Condition

The lateral open boundary condition for the selected nested-domain is implemented using the BDY module of NEMO. Two numerical algorithms are used to treat open boundary conditions depending on the prognostic simulated variables. The Flather scheme (Oddo and Pinardi., 2008) is used for barotropic velocities, while the flow relaxation scheme (Engedahl, 1995) is considered for baroclinic velocities, active tracers and sea surface height. In our formulation, we provide external data along straight open boundary lines, and the relaxation area is equal to one internal grid point. As the parent coarse resolution ocean model provides only the total velocity field, the interpolated total velocity field in the child grid is split into barotropic and baroclinic components. An integral constraint method is imposed to preserve the total transport after the interpolation.

This process involves the following steps:

1) defining the open boundary geometry (for each of the T, U and V grids) and physical fields (active tracers, sea-surface height, barotropic and baroclinic velocities) at the open boundary points using the geometry_bdy and fields_bdy procedures, respectively;

2) writing these data arrays to the files that are necessary to run the NEMO code.

The algorithms used for the different fields are the Flather radiation scheme for the barotropic velocities and the sea surface height and the Flow relaxation scheme for the baroclinic velocities and active tracers.

2.1.5 Integral Constraint at the open boundary

The downscaling is designed to ensure that the volume transport across the open boundary (OB) of the child model matches that across the corresponding section of the parent model.

At the eastern/western boundaries U-Points are imposed using the following conditions

$$\int_{y_2}^{y_1} \int_{-H_{child}}^{\eta_{child}} U_{child} dzdy = \int_{y_2}^{y_1} \int_{-H_{parent}}^{\eta_{parent}} U_{parent} dzdy \tag{2.3}$$

where y_1, y_2 are the extremes of the open boundary section; η_{child}, H_{child} are the surface elevation and the bathymetry of the child model at the boundary, respectively; $\eta_{parent}, H_{parent}$ are the surface elevation and the bathymetry of the parent model at the boundary, respectively; and U_{parent}, U_{child} are the parent/child total zonal velocities (normal velocity to the W/E boundaries).

The corrected velocity component normal to the boundary V_{child} is given (see N. Pinardi et al., 2003) by:

$$U_{child}(x, y, z, t) = U_{interp} - U_{correction} \tag{2.4}$$

where U_{interp} is the U_{parent} interpolated on the child open boundary points and the velocity correction is given by

$$U_{correction} = \frac{M_{interp} - M_{parent}}{S} \tag{2.5}$$

where $M_{interp} = \int_{y_2}^{y_1} \int_{-H_{child}}^{\eta_{child}} U_{interp} dzdy$ is the volume transport across the OB, the $M_{parent} = \int_{y_2}^{y_1} \int_{-H_{parent}}^{\eta_{parent}} U_{parent} dzdy$ is the volume transport across the corresponding OB and $S = \int_{y_2}^{y_1} \int_{-H_{child}}^{\eta_{child}} dzdy$ is the area of the section. These conditions are similarly imposed for the meridional velocity at the northern/southern boundaries (V-Points). The Integral Constraint procedure ensures that the interpolation does not modify the net transport across the child model lateral open boundary.

2.2 The NEMO ocean engine

NEMO is a community general circulation numerical model the uses finite differences to discretize the oceanic primitive equations. The range of application of NEMO is exceptionally wide, comprehending operational forecasts and ocean reanalysises, decadal predictions and longer time ranges. The physical equations and some key physical submodel (mainly vertical mixing parameterizations) are synthesized in the next sections in order to clarify our modeling choices and better our physical interpretations.

2.3 The oceanic primitive equations

The ocean is a fluid that can be described to a good approximation by the primitive equations, i.e. the Navier-Stokes equations along with a nonlinear equation of state which couples the two active tracers (temperature and salinity) to the fluid velocity, plus the following additional assumptions made from scale considerations:

- Spherical Earth approximation: we assume the geopotential surfaces to be spheroids that follow the Earth's bulge; we approximate these spheroids by spheres with gravity parallel to the Earth's radius and independent of latitude (White et al., 2005)

- Thin-shell approximation: we assume gravitational force and Coriolis terms independent from the depth since the ocean depth is negligible compared to the earth's radius.

- Turbulent closure hypothesis: the turbulent fluxes (which represent the effect of small scale processes on the large-scale) are expressed in terms of large-scale features

- Boussinesq hypothesis: we neglect density variations except in their contribution to the buoyancy force
$$\rho = \rho \left(T, S, p\right) \tag{2.6}$$

- Hydrostatic hypothesis: we simplify the vertical momentum equation, obtaining a balance between the buoyancy force and the vertical pressure gradient (this neglects convective processes from the initial Navier-Stokes equations and so these processes must be elaborated independently)

$$\frac{\partial p}{\partial z} = -\rho g \tag{2.7}$$

- Incompressibility hypothesis: the divergence of the velocity vector U is assumed to be zero.

$$\nabla \cdot U = 0 \tag{2.8}$$

- Ignore additional Coriolis terms: the variation of the Coriolis terms depending on the cosine of latitude are neglected.

Because the gravitational force is so dominant in the equations of large-scale motions, made sense to choose an orthogonal set of unit vectors (i, j, k) linked to the Earth such that k is the local upward vector and (i, j) are two vectors orthogonal to k, i.e. tangent to the geopotential surfaces. Therefore are defined the following variables: U the vector velocity,

$\vec{U} = \vec{U}_h + w_k$

(the subscript h denotes the local horizontal vector, i.e. over the (i, j) plane), T the potential temperature, S the salinity, ρ the in situ density . The vector invariant form of the primitive equations in the (i, j, k) vector is the following:

The momentum balance:

$$\frac{\partial \vec{U}_h}{\partial t} = -[(\nabla \times \vec{U}) \times \vec{U} + \frac{1}{2}\nabla(U^2)]_h - fk \times \vec{U}_h - \frac{1}{\rho_0}\nabla_h + D^u + F^u \tag{2.9}$$

The heat and salt conservation equation

$$\frac{\partial T}{\partial t} = -\nabla \cdot (T\vec{U}) + D^T + F^T \tag{2.10}$$

$$\frac{\partial S}{\partial t} = -\nabla \cdot (S\vec{U}) + D^S + F^S \tag{2.11}$$

where ∇ is the generalised derivative vector operator in (i, j, k) directions, t is the time, z is the vertical coordinate, ρ is the in situ density given by the equation of state, ρ_0 is a reference density, p the pressure, f is the Coriolis acceleration (where is the Earth's angular velocity vector), and g is the gravitational acceleration. D^U, D^T and D^S are the parameterizations of small-scale physics for momentum, temperature and salinity, and F^U, F^T and F^S are the air-sea fluxes of momentum, heat and salinity.

2.4 Vertical Boundary Counditions

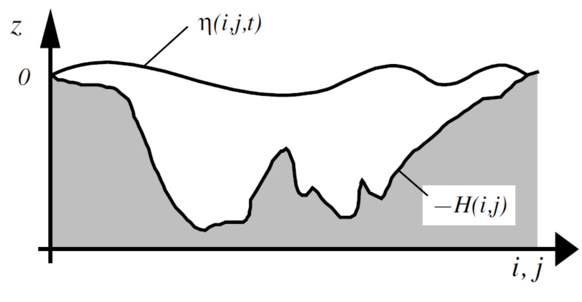

Figure 2.5: The ocean is bounded by two surfaces, $z = -H(i,j)$ and $z = \eta(i,j,t)$, where H is the depth of the sea floor and η the height of the sea surface. Both H and η are referenced to z = 0.

The ocean vertical fluxes can be summarized in two categories:

- bottom topography at the ocean's base,

- an air-sea or ice-sea interface at the ocean's top.

These boundaries can be defined by two surfaces, $z = -H(i,j)$ and $z = \eta(i,j,k,t)$, where H is the depth of the ocean bottom and η is the height of the sea surface. Both H and η are referenced to a surface of constant geopotential (i.e. a mean sea surface height) on which $z = 0$.

Through these two boundaries, the ocean exchanges fluxes of momentum, fresh water, heat and salt with the solid earth, the sea ice and the atmosphere. Nonetheless, some of these fluxes are so weak that even on climatic time scales they can be neglected.

To be more specific, we briefly discuss the vertical fluxes exchanged at the interfaces between the ocean and the other components of the earth system.

Bottom Solid earth - ocean: Heat and salt fluxes through the sea floor are small, except in special areas with specific characteristics. Therefore they are usually neglected in the model and the boundary condition is thus set to no flux of heat and salt through bottom solid boundaries. About momentum, the situation is different: since there is no flow across solid boundaries the velocity normal to the ocean bottom and coastlines is zero and the bottom velocity is thus parallel to solid boundaries. This kinematic boundary condition can be expressed as:

$$w = -U_h \cdot \nabla_h(H) \tag{2.12}$$

Moreover exchange of momentum is also due to frictional processes with the earth. This transfer of momentum occurs at small scales inside the boundary layer and, therefore, is described in terms of turbulent fluxes using bottom and lateral boundary conditions, depending on the physical parameterization in the equation of the momentum balance.

Atmosphere - ocean: The mass flux of fresh water PE (the precipitation minus evaporation budget) togheter with the kinematic surface condition leads to:

$$w = \frac{\partial \eta}{\partial t} + \vec{U}_h|_{z=\eta} \cdot \nabla_h(\eta) + P - E \tag{2.13}$$

Neglecting the surface tension and with it the insignificant capillary waves, the dynamic boundary condition leads to the continuity of pressure across the interface $z = \eta$. Of course there also are exchanges between the two media of horizontal momentum, due to the wind stress and exchange of heat, with net downward heat fluxes Q_{net} calculated as:

$$Q_{net} = Q_{SW} - Q_{LW} - Q_{lat} - Q_{sen} \tag{2.14}$$

where Q_{SW} is the incoming short wave radiation, Q_{LW} is the exiting long wave radiation, Q_{sen} is the exiting sensible heat balance and Q_{SW} is the exiting latent heat balance.

2.5 Subgrid scale physics

The hydrostatic primitive equations describe the behaviour of a geophysical fluid at space and time scales larger than a few kilometres in the horizontal, a few meters in the vertical and a few minutes. They are usually solved at larger scales: the specified grid spacing and time step of the numerical model. The effects of smaller scale motions (coming from the previously neglected advective terms in the Navier-Stokes equations) must be represented independently in terms of large-scale fields and forcing to close the equations. These effects appear in the equations as the divergence of turbulent fluxes (i.e. fluxes associated with the mean correlation of small scale perturbations). The necessity to choose a formulation of these turbulent fluxes corresponds to the necessity to assume a turbulent closure hypothesis. That's usually called the subgrid scale physics. Is important to consider that, even if this is the weakest part of the primitive equations, is also one of the most important for long-term simulations since small scale processes balance the surface input of kinetic energy and heat. Considering that the control exerted by gravity on the flow induces a strong anisotropy between the lateral and vertical motions, the subgrid-scale physics D^U, D^S and D^T in equation (2.9), equation (2.10) and equation (2.11) are necessarily divided into a lateral part D^U, D^S and D^T and a vertical part D^vU, D^vS and D^vT . The formulation of these terms and their underlying physics are briefly discussed in the next two subsections.

2.5.1 The lateral diffusive and viscous operators

Lateral turbulence can be fundamentally divided into two phenomenologically separate parts:

- a mesoscale turbulence associated with eddies (which can be solved explicitly if the resolution is sufficient since their underlying physics are included in the primitive equations),
- a sub mesoscale turbulence which is never explicitly solved even partially, but always parameterized.

The formulation of lateral eddy fluxes depends on whether the mesoscale is below or above the grid-spacing.
In non-eddy-resolving configurations,like the EAS5 father model, the closure is analogous to the one used for the vertical physics. The lateral turbulent fluxes are calculated to approximating a linear dependency on the lateral gradients of large-scale quantities. The resulting lateral diffusive and dissipative operators are of second order. It is well known from previous observations that lateral mixing induced by mesoscale turbulence tends to be along isopycnal surfaces (or more precisely neutral surfaces McDougall (1987)) rather than across them; since the slope of neutral surfaces is small in

the ocean, a reasonable approximation is to assume that the "lateral" direction is the horizontal, this means that the lateral mixing is performed along geopotential surfaces. This brings us to a geopotential second order operator for lateral subgrid scale physics. However this assumption can be relaxed: the eddy-induced turbulent fluxes can be better approached by assuming that they depend linearly on the gradients of large-scale quantities computed along neutral surfaces where the diffusive operator is an isoneutral second order operator and it has components in the three space directions. However, both horizontal and isoneutral operators have no effect on mean (i.e. large scale) potential energy, through baroclinic instabilities, conversely potential energy is a main source of turbulence.

An alternative parameterisation of mesoscale eddy-induced turbulence was proposed from (Gent and Mcwilliams, 1990), associating an eddy-induced velocity to the isoneutral diffusion. This parameterisation, used in our experiments, reduces the mean potential energy of the ocean leading to a formulation of lateral subgrid-scale physics made up of an isoneutral second order operator and an eddy induced advective part. Since there is no really satisfactory formulation of the lateral eddy coefficients as a function of large-scale features, the specification of these coefficients is the key point in all these lateral diffusive formulations. In eddy-resolving configurations, a second order operator can be used, but usually the more scale selective biharmonic operator is preferred as the grid-spacing is usually not small enough compared to the scale of the eddies. The role interpreted from the subgrid-scale physics is to dissipate the energy that, as well known from (Kolmogorov, 1941), cascades to the little, not resolved scales, where is finally dissipated; thus this besides from giving an adequate modeling of the dissipation phenomena, also ensures the stability of the model while not interfering with the resolved mesoscale activity. Another, less physical, approach is becoming more and more popular: instead of specifying explicitly a sub-grid scale term in the momentum and tracer time evolution equations, one uses an advective scheme which is diffusive enough to maintain the model stability. It must be emphasised that then, all the sub-grid scale physics is included in the formulation of the advection scheme. All these parameterizations of subgrid scale physics have advantages and drawbacks. For active tracers (temperature and salinity) the main ones are: Laplacian and bilaplacian operators acting along geopotential or iso-neutral surfaces, (Gent and Mcwilliams, 1990) parameterisation, and various slightly diffusive advection schemes. For momentum, the main ones are: Laplacian and bilaplacian operators acting along geopotential surfaces, and UBS advection schemes when flux form is chosen for the momentum advection. Since the goal of this thesis is to compare different Turbulent Closure Models (TCM), in this aspect we always tended to choose the same parameterization of the father model in order to isolate the dependency from the TCMs rather then the best performing model; therefore for active tracers, as for momentum were chosen slightly diffusive bilaplacian operators acting along geopotential surfaces, as were for the father EAS5 model.

2.5.2 Vertical subgrid scale physics

The model resolution necessarily excludes the major sources of vertical turbulence occur (shear instability, internal wave breaking...) and turbulent motions are not explicitly solved but always parameterized. The vertical turbulent fluxes are assumed to depend linearly on the gradients of mean-field quantities (for example, the turbulent heat flux is given by $T'w' = -A_{vt}\partial zT$, where A_{vT} is an eddy coefficient). Since the molecular viscosity acting on large scale underestimates the turbulent diffusion and dissipation and an ad hoc modeling of the details of turbulent motions is simply impractical, the formulation of turbulent diffusion and dissipation are analogous.
The resulting vertical momentum and tracer diffusive operators are of second order:

$$D^{vU} = \frac{\partial}{\partial z}(A^{vm}\frac{\partial \vec{U}_h}{\partial z}) \tag{2.15}$$

$$D^{vT} = \frac{\partial}{\partial z}(A^{vT}\frac{\partial T}{\partial z}) \tag{2.16}$$

and

$$D^{vS} = \frac{\partial}{\partial z}(A^{vS}\frac{\partial S}{\partial z}) \tag{2.17}$$

where A^vT and A^vm are the vertical eddy diffusivity and viscosity coefficients, respectively.

The the eddy coefficients impact largely all the vertical physics; their parameterization are based on different hypothesises that can be divided in the following assumptions:

- constant coefficients
- the coefficients are function of the local fluid properties (e.g. Richardson number, Brunt-Vaisala frequency, distance from the boundary...)
- the coefficients are computed from a turbulent closure model

In our specific case we are confronting a Richardson number dependent submodel with two turbulent closure submodels, in particular a $k-\epsilon$ closure model and a TKE (Turbulent Kinetic Energy) closure model. All of them will be described comprehensively in the following section 2.6.

2.6 Vertical mixing parameterizations

The models that we are going to compare are the commonly used, Richardson Number Dependent closure scheme, the more evolute, wave breaking considering,TKE closure scheme and the GLS turbulent scheme, more flexible, two-equation-based and still taking account of the Langimour Corrections over the Turbolent Kinetic Energy equation. Furthermore we are going to consider the effect of a double diffusion scheme in several case, and his effect on the simulation's accuracy. Finally we will briefly discussed the enhanced diffusion parameterization of the vertical instabilities.

2.6.1 Richardson Number Dependent submodel

In this case the vertical mixing coefficients are diagnosed from the large scale variables computed by the model. This correlation is based on in situ measurements that linked vertical turbulent activity to large scale ocean structures. The hypothesis of a mixing maintained by Kelvin-Helmholtz like instabilities leads to a dependency between the vertical eddy coefficients and the local Richardson number, that express the ratio of stratification to vertical shear.

$$Ri = \frac{N^2}{(\frac{\partial U_h}{\partial z})^2} \tag{2.18}$$

the following formulation has been implemented for the vertical eddy viscosity and diffusivity:

$$A^{vt} = \frac{A^{vt}_{ric}}{(1+aRi)^n} + A^{vt}_b \tag{2.19}$$

$$A^{vm} = \frac{A^{vt}_b}{(1+aRi)} + A^{vm}_b \tag{2.20}$$

where Ri is the local Richardson number, N is the local Brunt- Vaisala frequency, A^{vt}_b and A^{vm}_b are the constant background values set as in the constant case , and $A^{vt}_{ric} = 10^4 m^2/s$ is the maximum value that can be reached by the coefficient when Ri is positive, a = 5 and n = 2.

2.6.2 TKE turbulent closure scheme

The vertical eddy viscosity and diffusivity coefficients are computed from a Turbulent Kinetic Energy equation based closure model, constituted by a prognostic equation for TKE, and a closure assumption for the turbulent length scales. This turbulent closure model has been developed in the atmospheric case, then adapted for the oceanic case. The time evolution of TKE is the result of the production through vertical shear, the destruction through stratification, the vertical diffusion, and the dissipation:

$$\frac{\partial q}{\partial t} = \frac{K_m}{e_3^2}[(\frac{\partial u}{\partial k})^2 + (\frac{\partial v}{\partial k})^2] - K_p N^2 + \frac{1}{e_3}\frac{\partial}{\partial k}[\frac{A^{vm}}{e_3}\frac{\partial q}{\partial k}] - c_\epsilon \frac{q^{3/2}}{l_\epsilon} \tag{2.21}$$

$$K_m = C_k l_k \sqrt{q} \tag{2.22}$$

$$K_p = A^{vm}/P_{rt} \tag{2.23}$$

q is the TKE, N is the local Brunt Vaisala frequency, l_ϵ and l_k are the dissipation and the mixing length scales, P_{rt} is the Prandl number, K_m and K_p are the vertical eddy viscosity and diffusivity coefficients. The constants $C_k = 0.1$ and $C_\epsilon = 0.7$

The Prandl number is a function of the local Richardson number Ri.

$$P_{rt} = \begin{cases} 1 & \text{if } Ri < 0.2 \\ 5Ri & \text{if } 0.2 < Ri < 2 \\ 10 & \text{if } Ri > 2 \end{cases}$$

At the sea surface, the value of TKE is prescribed from the wind stress field as

$$q_{(z=0)} = \frac{e_{bb}|\tau|}{\rho_0} \tag{2.24}$$

Where e_{bb} instead of the default value of 3.75 proposed by (Gaspar et al., 1990) was set on a much larger value: 67.83 to take into account the surface wave breaking (section 2.6.2).

Turbulent lenght scale

For computational efficiency, the original formulation of the turbulent length scales proposed by (Gaspar et al., 1990) has been simplified basing on the following first order approximation (Blanke and Delécluse, 1993):

$$l_k = l_\epsilon = \sqrt{2\frac{q}{N}} \tag{2.25}$$

which is valid in a stable stratified region with constant values of the Brunt-Vaisala frequency. The resulting length scale is bounded by the distance to the surface or to the bottom or by the local vertical scale factor).

Blanke and Delécluse, 1993 notice that this simplification has two major drawbacks: it makes no sense for locally unstable stratification and the computation no longer uses all the information contained in the vertical density profile.

Surface Wave Breaking Parametrization

Following (Mellor and Blumberg, 2004), the TKE turbulence closure model has been modified including the effect of surface wave breaking energetics. This causes a reduction of summertime surface temperature when the mixed layer is relatively shallow.

The (Mellor and Blumberg, 2004) modifications acts on surface length scale and TKE values and air-sea drag coefficient. Following (Craig and Banner, 1994), the boundary condition on surface TKE value is :

$$q_0 = \frac{|\tau|}{\rho_0}(15.8 * \alpha_{cb})^(2/3) \tag{2.26}$$

where α_{CB} is the (Craig and Banner, 1994) constant of proportionality which depends on the "wave age", ranging from 57 for mature waves to 146 for younger waves (Mellor and Blumberg, 2004). The boundary condition on the turbulent length scale follows the Charnock's relation:

$$l_0 = k\beta\frac{|\tau|}{g\rho_0} \tag{2.27}$$

where k = 0.40 is the von Karman constant, and β is the Charnock's constant. (Mellor and Blumberg, 2004) suggest $\beta = 2.105$ the value chosen by (Stacey, 1999) citing observation evidence, and $\alpha_{CB} = 100$ the Craig and Banner's value. A minimal threshold $q_0^{min} = 10^{-4}[\frac{m^2}{s^2}]$is applied on the surface value.

Langimour Cells

Langmuir circulation (LC) are ordered large-scale vertical motions in the surface layer of the oceans. Although LC have nothing to do with convection, the circulation pattern is rather similar to so-called convective rolls in the atmospheric boundary layer. The main explanation of this phenomenon is that LC arise from a nonlinear interaction between the Stokes drift and wind drift currents. We utilized in the TKE turbulent closure a simple parameterization of Langmuir circulation following (Axell, 2002) tractation for a k-ϵ turbulent closure.
This parameterization results in an extra source term of TKE, P_{LC} . By making an analogy with the characteristic convective velocity scale (D'Alessio et al., 1998), this additional source term is assumed to be :

$$P_{LC} = \frac{w_{LC}^3(z)}{h_{LC}} \tag{2.28}$$

where w_{LC}(z) is the vertical velocity profile of LC, and h_{LC} is the LC depth. With no information about the wave field, w_LC was assumed to be proportional to the Stokes drift $u_s = 0.377\ |\tau|^{1/2}$, where $|\tau|$ is the surface wind stress module. For the vertical variation, w_{LC} is assumed to be zero at the surface as well as at a finite depth h_{LC} (which is often close to the mixed layer depth), and simply varies as a sine function in between (a first-order profile for the Langmuir cell structures). The resulting expression for w_{LC} is :

$$w_{LC} = \begin{cases} u_s c_{LC} sin(-\pi z/h_{LC}) & \text{if } -z < h_{LC} \\ 0 & \text{if } -z > h_{LC} \end{cases}$$

where $c_{LC} = 0.15$ has been chosen by (Axell, 2002) as a good compromise to fit LES data but in general can be set between 0.15 and 0.54. The chosen value yields maximum vertical velocities w_{LC} of the order of a few centimeters per second. The h_{LC} computation is analogous to the turbulent length scale of TKE equations: h_{LC} is the depth to which a water parcel with kinetic energy due to Stoke drift can reach on its own by converting its kinetic energy to potential energy, according to

$$-\int_{-h_{LC}}^{0} N^2 z dz = \frac{1}{2} u_s^2 \tag{2.29}$$

2.6.3 Generic Length Scale

The Generic Length Scale (GLS) scheme is a turbulent closure submodel based on two prognostic equations: one for the turbulent kinetic energy (TKE), and another for the generic length scale, ψ. This variable is defined as:

$$\psi = C_o \mu^p q^m l^n \tag{2.30}$$

where the (p; m; n) values allows to recover a number of well-known turbulent closures (k-kl , k- ϵ , k-ω among others). The GLS scheme is constituted by the following set of equations:

$$\begin{aligned}
&\tfrac{\partial q}{\partial t} = \tfrac{K_m}{\sigma_e e_3}[(\tfrac{\partial u}{\partial k})^2(\tfrac{\partial v}{\partial k})^2] - K_p N^2 + \tfrac{1}{e_3}\tfrac{\partial}{\partial k}[\tfrac{K_m}{e_3}\tfrac{\partial q}{\partial k}] - \epsilon \\
&\tfrac{\partial \psi}{\partial t} = \tfrac{\psi}{q}\left[\tfrac{C_1 K_m}{\sigma_\psi e_3}[(\tfrac{\partial u}{\partial k})^2(\tfrac{\partial v}{\partial k})^2] - C_3 K_p N^2 - C_2 \epsilon F w\right] + \tfrac{1}{e_3}\tfrac{\partial}{\partial k}[\tfrac{K_m}{e_3}\tfrac{\partial \psi}{\partial k}] - \epsilon \\
&K_m = C_\mu \sqrt{q} l \\
&K_p = C_{\mu'} \sqrt{q} l \\
&\epsilon = C_0 \tfrac{q^{3/2}}{l}
\end{aligned} \tag{2.31}$$

where N is the local Brunt-Vaisala frequency, q is the turbulent kinetic energy (TKE) and ϵ the dissipation rate ($\frac{\partial q}{\partial t}$. The constants C_1, C_2, C_3, σ_e e, σ_ψ and the wall function (Fw) depends of the choice of the turbulence model. C_μ and $C_{\mu'}$ are calculated from the stability function. The value of $C_{0\mu}$ depends of the choice of the stability function. The surface and bottom boundary condition on both TKE and ψ can be calculated thanks to Dirichlet or Neumann condition. As for TKE closure , the wave effect on the mixing is considered adding an additional term to the TKE equation. The equation is known to fail in stably stratified flows, and for this reason almost all authors apply a clipping of the length scale as an ad hoc remedy. With this clipping, the maximum permissible length scale is determined by

$$l_{max} = c_{lim} \tag{2.32}$$

Where, following (Galperin et al., 1988), a value of clim = 0.53 was used.

2.6.4 Double Diffusion Mixing

Double diffusion mixing occurs when relatively warm, salty water lies over cooler, fresher water, or vice versa.
This conditions lead to salt fingering diffusive convection, contributing to diapycnal mixing in extensive regions of the ocean. Merryfield et al., 1999 include a parameterization of these phenomena in a global ocean model and show that it leads to relatively minor changes in circulation but deploys significant regional influences on temperature and salinity. Diapycnal mixing of S and T are modeled with diapycnal diffusion coefficients

$$A^{vT} = A_0^{vT} + A_f^{vT} + A_d^{vT} \tag{2.33}$$

$$A^{vS} = A_0^{vS} + A_f^{vS} + A_d^{vS} \tag{2.34}$$

where subscript d represents mixing by diffusive convection, f by salt fingering, and 0 by processes other than double diffusion.
The double-diffusive mixing is related to the buoyancy ratio $R_\rho = \alpha\ \partial_z$ T$/\beta\ \partial_z$S, where α and β are coefficients of thermal expansion and saline contraction. To take account of the mixing of S and T by salt fingering, we adopt the diapycnal diffusivities, following (Schmitt, 1981):

$$\begin{array}{l} A_f^{vS} = (\frac{A^{*v}}{R_p/R_c})^n \quad \text{if } R_p > 1 and N^2 > 0 \\ A_f^{vS} = 0 \quad \text{otherwise} \\ A_f^{vT} = 0.7 A_f^{vS}/R_p \end{array} \tag{2.35}$$

As suggested in (Merryfield et al., 1999), we adopted $R_C = 1.6$, n = 6, and $A^{*v} = 10^{-4}$ m^2/s.
Similarly to represent mixing of S and T by diffusive layering, were the diapycnal diffusivities following (Federov, 1988) , with a linear linear dependence between diffusivities and an exponential dependence over R_p.

2.6.5 Enhanced diffusion

In this case, the vertical eddy mixing coefficients are assigned very large values in regions where the stratification is gravitationally unstable (when N^2 the Brunt-Vaisala frequency is negative) (Lazar, 1997).

In practice, where $N^2 \leq 0$, A_T^{vT}

where A_T^{vS} is set equal to typical values between 1 and 100 m^2/s, in our case 10 m^2/S. This is the simplest, less time consuming parameterization for vertical processes. Despite his simplicity it is widely used, especially with simple turbulent closures like constant coefficients or Pacanovski-Philander closure scheme.

Chapter 3

Control experiment

The CMCC's Med-Currents system a reliable and widely used circulation forecasting model to nest higher resolution models (Trotta et al., 2016). In our case we have chosen the latest version of the system so-called EAS5, that gives daily mean temperature, salinity sea level and velocity fields from 2016 to today.

3.1 Description of the Med-Currents EAS5 model system

The Mediterranean Forecasting System, MFS, (N. Pinardi et al., 2003;Pinardi and Coppini, 2010; Tonani et al., 2014) is providing, since year 2000, analysis and short-term forecast of the main physical parameters in the Mediterranean Sea and it is the physical component of the Med-Monitoring and Forecasting Center called Med-Currents. The MFC is the infrastructure of the Copernicus Marine Environment Monitoring Service that produces ocean forecasts for the global ocean and the European regional seas. The analysis and forecast Med-Currents system at EAS5 is provided by means of a coupled hydrodynamic-wave model implemented over the whole Mediterranean basin and extended into the Atlantic Sea in order to better resolve the exchanges with the Atlantic Ocean at the Strait of Gibraltar.

The model solutions are corrected by the variational assimilation of temperature and salinity vertical profiles and along track satellite Sea Level Anomaly observations.

The Med-Currents system is composed of several sub-components, that is:

- An Upstream Data Acquisition system, Pre-Processing and Control of: ECMWF atmospheric forcing fields from analysis and forecast, Satellite (SLA and SST) and in-situ (T and S) data profiles.
- A Forecast/Simulation component: NEMO-WW3 modelling system is run to produce one day of simulation and 10 day forecast.

- Analysis/Simulation component: NEMO-WW3 modelling system is combined with a 3D assimilation scheme in order to produce the best sea analysis. The NEMO+WW3+3D-Var system is running for 15 days into the past in order to use the best available along track SLA products. The latest day of the 15 days of analyses, produces the initial condition for the 10-day forecast.

- Post processing component: the model output is processed in order to get the products for the CMEMS catalogue.

3.1.1 Circulation model component

NEMO has been implemented in EAS5 on a 1/24° x 1/24° horizontal staggered grid with 141 unevenly spaced vertical levels (Clementi et al., 2017) with time step of 240sec. The advection scheme for active tracers, temperature and salinity, is a mixed up-stream/MUSCL (Monotonic Upwind Scheme for Conservation Laws; Leer, 1979), originally implemented by (Oddo et al., 2009). The vertical diffusion and viscosity terms are a function of the Richardson number as parameterized by (Pacanowski and Philander, 1981). The air-sea bulk formulae implemented currently are described in (Pettenuzzo et al., 2010). (Oddo et al., 2009) and (Oddo et al., 2014) give a detailed description of other specific features of the model implementation. The vertical background viscosity and diffusivity values are set to $1.2 \cdot 10^{-6}$ $[m^2/s]$ and $1.0 \cdot 10^{-7}$ $[m^2/s]$ respectively, while the horizontal bilaplacian eddy diffusivity and viscosity are set respectively equal to $-1.2 \cdot 10^8$ $[m^4/s]$ and -2.0 $\cdot 10^8$ $[m^4/s]$. A quadratic bottom drag coefficient with a logarithmic formulation has been used and the model utilizes vertical partial cells to fit the bottom depth shape. The hydrodynamic model is nested in the Atlantic within the Global analysis and forecast system daily data set (1/12° horizontal resolution, 50 vertical levels) that is interpolated onto the MedCurrents model grid. (Oddo et al., 2009) shows details on the nesting technique and major impacts on the model results. The model forcing, coming from momentum, water and heat fluxes is interactively computed by bulk formulae using the 1/10° horizontal-resolution operational analysis and forecast fields from the European Centre for Medium-Range Weather Forecasts (ECMWF) at highest available time frequency (1 hour for the first 3 days of forecast, 3 hours for the following 3 days of forecast and 6 hours for the last 4 days of forecast and for the analysis). The water balance is computed as Evaporation minus Precipitation and Runoff. The runoff of the 39 rivers is given by monthly mean datasets. The Dardanelles Strait is implemented as a lateral open boundary condition by using GLO-MFC daily Analysis and Forecast product and daily climatology derived from a Marmara Sea box model (Maderich et al., 2015). The topography component is computed starting from the GEBCO 30arc-second grid filtered (using a Shapiro filter) and manually modified in critical areas such as: islands along the Eastern Adriatic coasts, Gibraltar and Messina straits, Atlantic box edge.

Morover EAS5 uses a a three-dimensional variational data assimilation scheme developed by (Srdjan and Pinardi, 2008) and modified by (Storto et al., 2015). The assimilated data include: along track Sea Level Anomaly from CLS SL-TAC, and insitu vertical temperature and salinity profiles from VOS XBTs (Voluntary Observing Ship-eXpandable Bathythermograph) and ARGO floats.

3.2 Control experiment

The Control experiment has the purpose to evaluate the grid resolution effects and to constitute a reference for the comparison with the study cases where in additon to the horizontal resolution, the vertical mixing schemes are changed.
Since our study is centered on the mixed layer also the vertical grid of Control was changed to improve the resolution of the mixed layer.
All the EAS5 settings are left the same except for the few that we describe.
NEMO has been implemented in the Control on a 1/72° x 1/72° horizontal staggered grid with 141 unevenly spaced vertical levels (Clementi et al., 2017) with time step of 240sec.
The vertical background viscosity and diffusivity values are set to $1.2 \cdot 10^{-6}$ $[m^2/s]$ and $1.0 \cdot 10^{-7}$ $[m^2/s]$ respectively, while the horizontal bilaplacian eddy diffusivity and viscosity are set respectively equal to $-1.5 \cdot 10^6$ $[m^4/s]$ and $-2.6 \cdot 10^6$ $[m^4/s]$.
The hydrodynamic model is nested in EAS5 system that is interpolated onto the Med-Currents model grid. The model forcing, coming from momentum, water and heat fluxes is interactively computed by bulk formulae using the 1/10° horizontal-resolution operational analysis and forecast fields from the European Centre for Medium-Range Weather Forecasts (ECMWF).

3.3 The Control domain

The geographical domain covers a section of the Levantine Sea from 33.33°E to 35.27°E, and from 33.15°N to 35.27°N. The horizontal resolution is 1/72° in both latitude and longitude directions. This was the smallest box possible containing an intense gyre developed in that zone, the high resolution, triple with respect to the father model, and the domain choice are due to the focus of our experiments, the developing of a better mixed layer modeling in a case of strong anticyclonic vorticity center. Moreover, as previously stated, the Levantine basin is a zone of particular interest due to the process of intermediate water formation that influences all Mediterranean circulation.

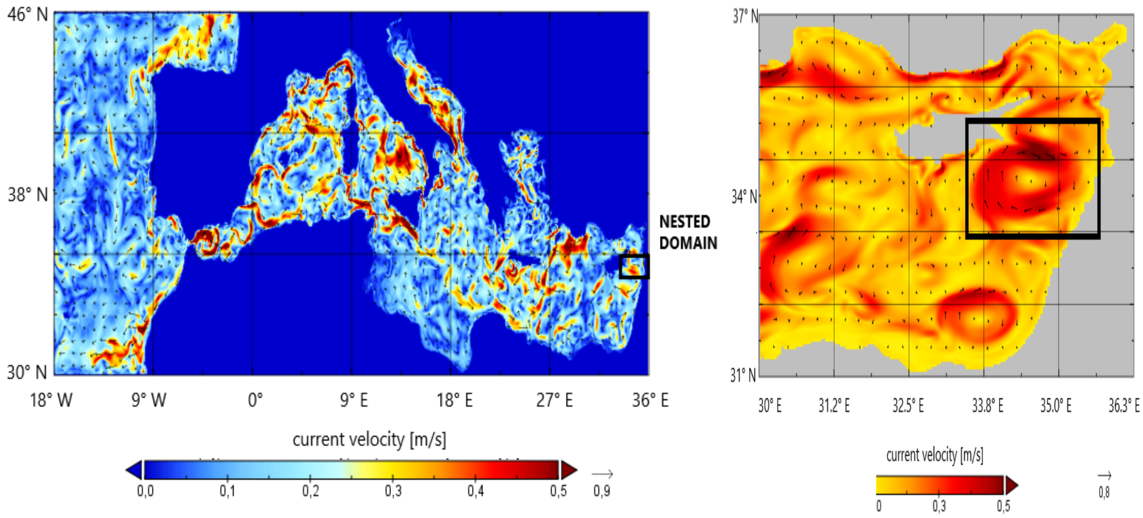

Figure 3.1: Left panel: Control domain, nested in EAS5, in particular EAS5 daily mean current velocity plot of 01/10/2020.
To the right EAS5 04/10/2020 daily mean current velocity and current amplitude plot.

3.3.1 Vertical grid

We impose 141 vertical levels from the surface to a maximum depth of 2600 m, and the corresponding thickness varyes from 0.5 m at the top to 30 m in the deepest layer.

Since previous EAS5 results show a Mixed Layer Depth around 30 meters in order to improve our representation of the ML most of the 141 vertical depth levels should be concentrate near the surface. Both vertical grids are shown in Fig. 3.2 and are geopotential z-coordinate levels with partial bottom cell representation of the bathymetry. The parameters were set following three principles:

1) to invest most of ML, for the first 40 meter we set a vertical level each half meter

2) for the efficiency of the computation we should minimize the stretching of the parametric function (we want low values of the second derivative of the parametric function

3)the first level should be within the fist meter from the sea surface.

Following these principles we obtained the following parameterization

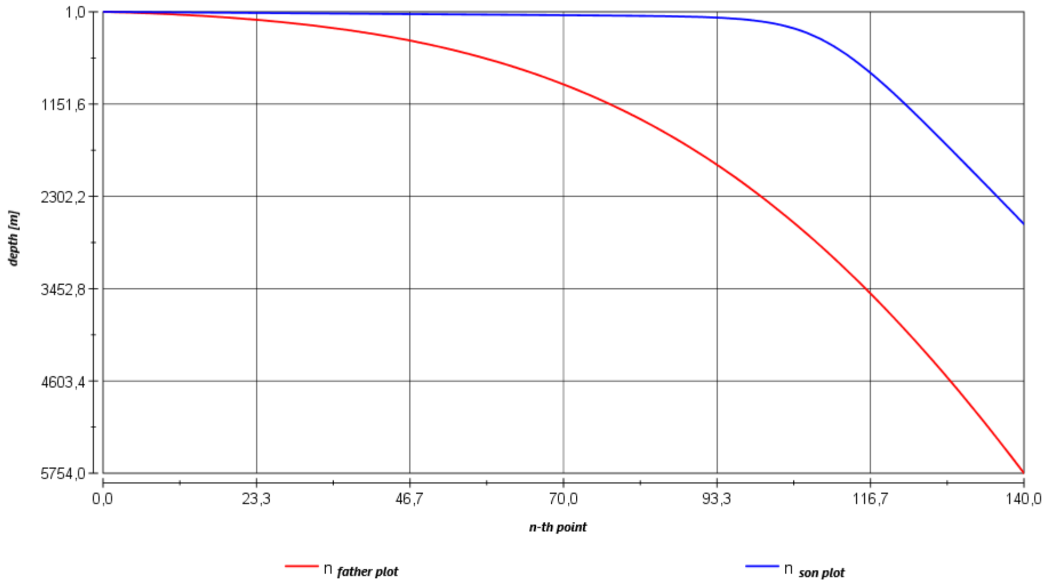

Figure 3.2: geopotential z-coordinate levels of the father and the sons domains

h_{sur}	-4370.9
h_0	42.6
h_1	42
h_{th}	111
h_{cr}	10

The father model follows the same parameterization but has less points in the top 100 meters of depth. In the Tab 3.1 we provide the following correspondence between the depth levels of the father and the son.

3.4 Comparison between EAS5 and Control experiments

The Control experiment has the purpose to evaluate the effect of the grid on the tracers and current velocity fields evolution. Can be noticed how apart from the horizontal

vertical level	father depth [m]	son depth [m]
5th	13.3	3.9
15th	51.4	9.9
25th	112.3	15.9
35th	203.2	21.9
45th	333.2	27.9
55th	513.3	33.9
65th	756.2	40.0
75th	1075.9	46.3
85th	1486.7	55.0
95th	2001.4	80.4
105th	2630.1	207.2
115th	3378.0	652.6
125th	4244.8	1396.4
135th	5524.7	2226.5

Table 3.1

and vertical grid, all the Control parameterization resembles the father model. The distribution of the vertical levels has been discussed in the previous chapter as well as the horizontal grid resulting in a much higher son model resolution, especially in the Mixed layer. In order to evaluate the quality of Control, as well as to analyze the effects of the grid, several comparisons between Control and EAS5 were made. The father fields and the son initial condition were verified to be identical (apart from grid interpolation effects). We analyzed current, temperature and salinity fields both horizontally and vertically as well as air-sea fluxes.

model	EAS5	Control
father model	GLOMFC	EAS5
horizontal resolution	1/24°	1/72°
number of z-levels	141	141
zonal domain	18.1 W - 36.3 E	33.33°E - 35.27°E
merid. domain	30.2 N - 46 N	33.15°N - 35.27°N
grid type	staggered Arakawa C-grid	staggered Arakawa C-grid
time average	24 h	1 h
Advection scheme	MUSCL	MUSCL
Lateral diffusion scheme (U,V)	bilaplacian along geopotential surface	bilaplacian along geopotential surface
Lateral diffusion scheme (T,S)	bilaplacian along geopotential surface	bilaplacian along geopotential surface
Air Sea Interaction Bulk formulation	MFS	MFS
atm forcing	EMCWF numerical weather prediction	EMCWF numerical weather prediction
MLE parameterization	no	yes
Boundary Condition	flather + Orlanski	flather
River runoff	yes	no
Variational assimilation	3D-VAR	no
Vertical, viscosity and diffusivity	Pacanowski Philander	Pacanowski Philander

3.4.1 Tracers and velocity fields

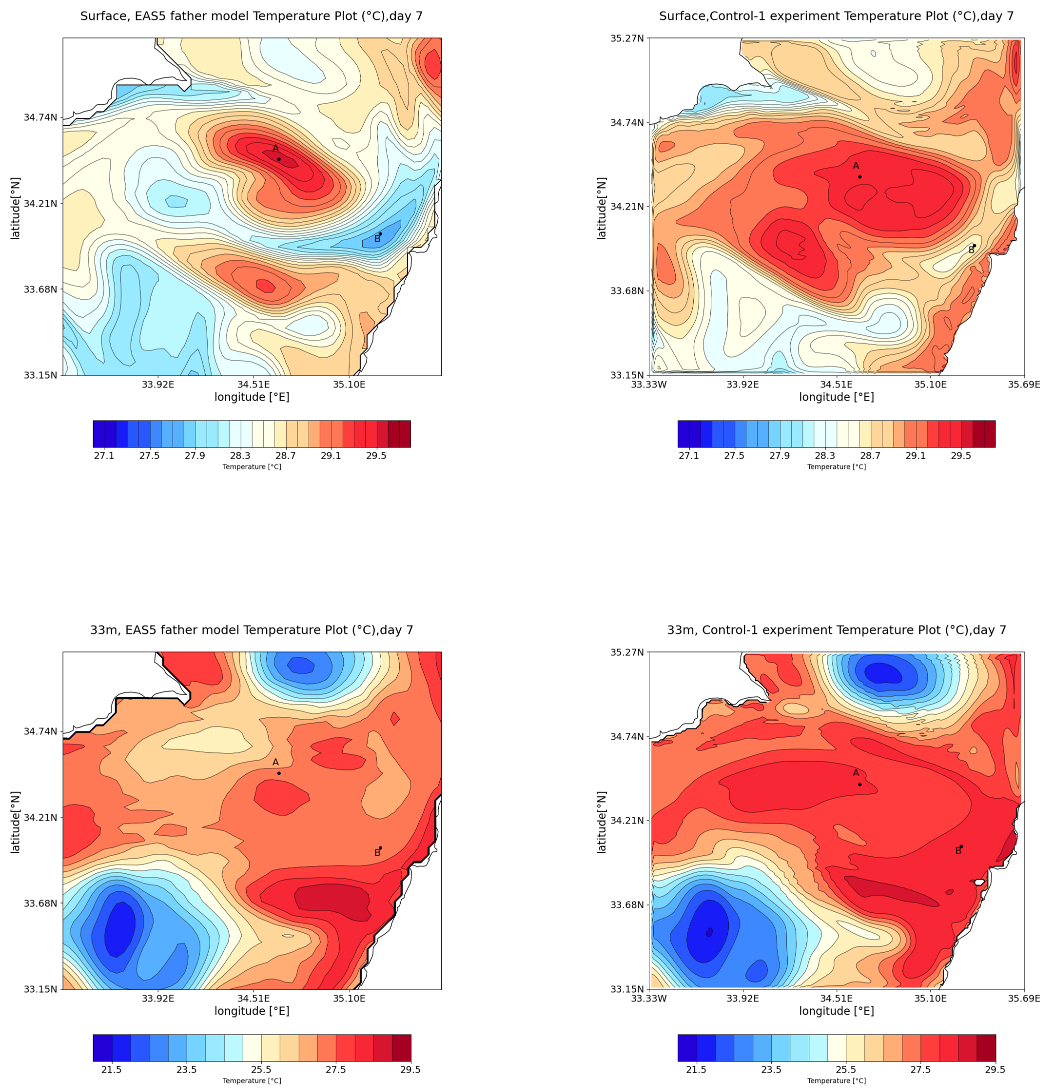

Figure 3.3: Top panels: EAS5 (left panel) and Control (right panel), surface temperature plots, daily mean on 07/10/2020.
Bottom panel: EAS5 (left panel) and Control (right panel), 33m depth temperature plots, daily mean on 07/10/2020.

The temperature horizontal comparison is shown in Figure 3.3, two horizontal levels were compared: the surface and 33 meters depth, that is just below the typical mixed layer depth as we observe from the vertical profiles. The points A and B, respectively having coordinates (34.39 N, 34.65 E) and (33.97 N 35.37 E), were chosen for the vertical profiles comparison, since these are the two points where the two fields most depart from each other. We can notice how at the surface observe the temperature has important differences structurally, being more uniform in the Control experiment: the EAS5 model has maximum values of 29.6°C and minimum of 27.7°C, Control highest values are instead lower than 29.5°C and the minima 27.9°C. The development of different convective structures due to a major grid resolution has already been observed (Trotta et al., 2017).
In the 33m depth comparison, just below the ML, we observe a different behaviour with lower temperature values in the cold structures in Control. In the nothern structure (around 34.7 E, 35.1 N) expecially, since EAS5 reaches minimum values of 23.4°C when Control reaches 23.2°C. This behaviour is probably correlated with an reinforcement of upward temperature advecting processes. Besides this zone, the Control experiment shows higher temperatures in most of the domain, often with differences between 0.4°C and 0.8°C. This behavior is strictly correlated with the deepening of the mixing layer in the Control with respect to EAS5, this is supported by the similarity between these temperature, often around the 28°C and the previously observed surface temperatures, and by the following Temperature vertical profiles comparison.

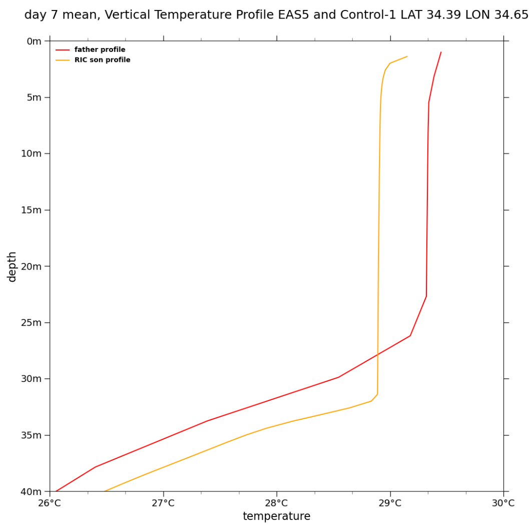

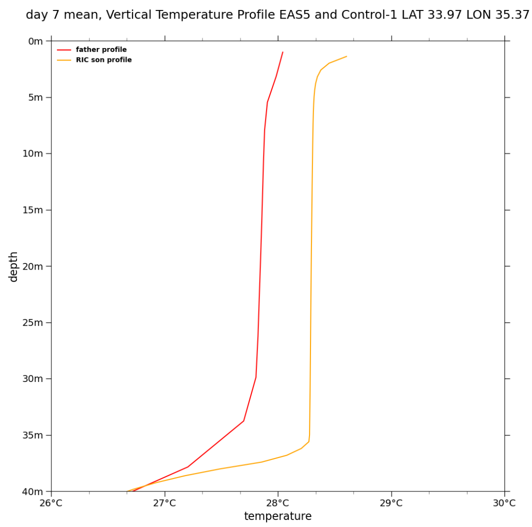

Figure 3.4: EAS5 and Control, vertical temperature plots, daily mean 7/10/2020, Point A 34.39 N 34.65 E (on the left) and Point B 33.97 N 35.37 E (on the right).

The vertical comparison of the daily mean temperature on 7/10/2020, in the locations A e B , Figure 3.4, show that, even if the considered points are extremely different in terms of superficial temperature, since in point A Control has an inferior superficial an ML temperature than EAS5 and in point B is the opposite, is quite significant to notice how in both cases (as well as in other profiles shown in the next chapter) the Control model develops a deeper mixed layer, the depth difference is significant and is aroud 5 m allover the domain. Is also curios to observe how in both cases the temperature vertical gradient of Control at the surface is much stronger than the EAS5 one, with the Control temperature in the mixed layer that changed strongly in the first couple of meters (about 0.3°C in the first case, about 0.5° in the second one), then remains almost constant in the mixed layer; EAS5 temperature instead changes much more gradually, probably because of his inferior vertical resolution in the first 50 m of depth, as seen in section 3.3.1.
The developing of a deeper mixed layer and in general the increasing of vertical processes is correlated to the different grid density probably due to the developing of a stronger vertical velocity This hypothesis is going to be further discussed in the Velocity field confront.

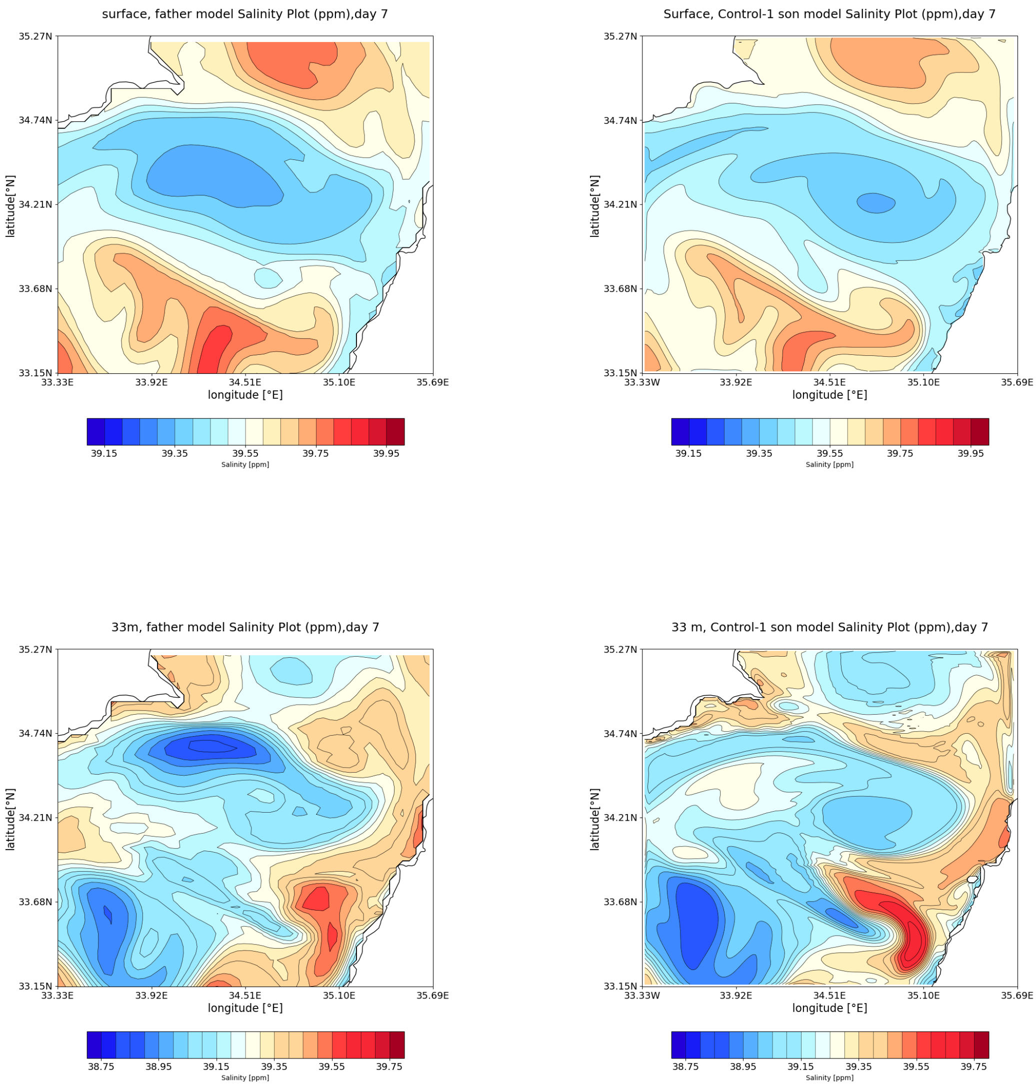

Figure 3.5: Top panels: EAS5 (left panel) and Control (right panel), surface salinity plots, daily mean on 07/10/2020.
Bottom panels: EAS5 (left panel) and Control (right panel), 33 m salinity plots, daily mean on 07/10/2020.

The horizontal salinity comparison in Figure 3.5 again was done on two horizontal levels: the surface one and the 33 m, below-the-ML one. This comparison confirm some of the observation made on the temperature: at the surface, structurally there are no such differences as observed in the temperature plot but again we can see a reduced gap between lower and higher values in the domain in the Control experiment, With the EAS5 model that reaches maxima over 40 PSU and minima under 39.35 PSU and Controls that goes from maxima around 39.95 PSU and minima under 39.4 PSU. These differences are less significant of the ones observed in the temperature comparison but help to recognise the generality of this behaviour strengthening the horizontal mixing hypothesis. At 33 m depth we observe quite similar fields, with the Control model that develops generally higher values than EAS5, especially in the central region, this can be explained again with the deepening of the ML, as well as with the vertical velocity comparison.

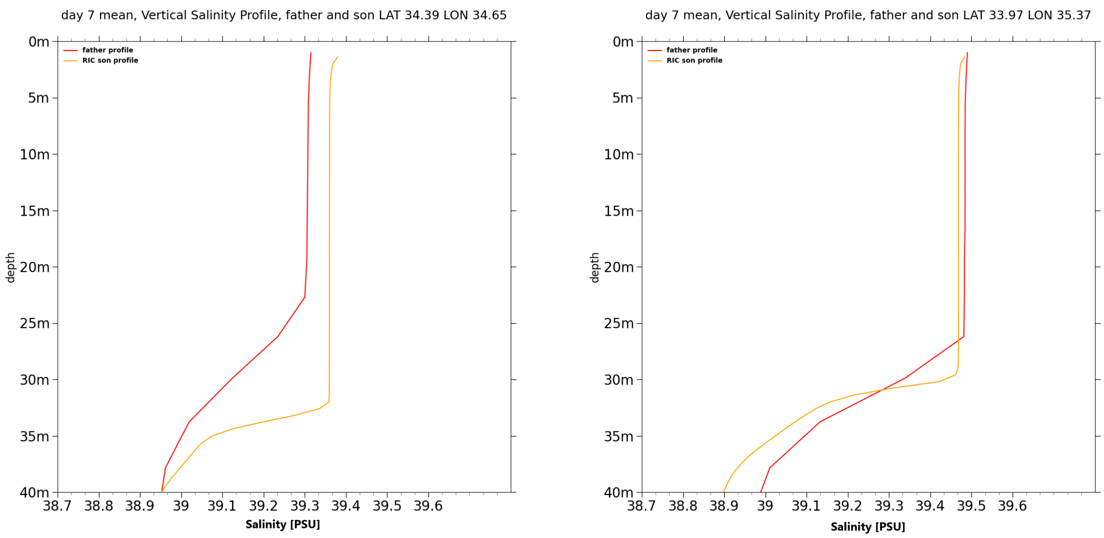

Figure 3.6: EAS5 and Control, vertical salinity plots, daily mean 7/10/2020, Point A 34.39 N 34.65 E (on the left) and Point B 33.97 N 35.37 E (on the right).

We compared the vertical salinity profile in the points A and B previously discussed. In Fig. 3.6 we can observe a deeper mixed layer in both cases (in particular in the first one), independently on the reached values, also is interesting to notice ho the profile just below the mixed layer is much steeper in the Control experiments, probably thanks to the much denser vertical grid in the first 50 m of ocean. We can also notice how the difference between the models, reduced at the surface grow and reach their maximum at the base of the mixed layer. This comparison again confirms what observed in the temperature one.

The velocity comparison, Figure 3.7, shows a great resemblance between the two fields, with the most noticeable differences in the maximum velocities in the zone

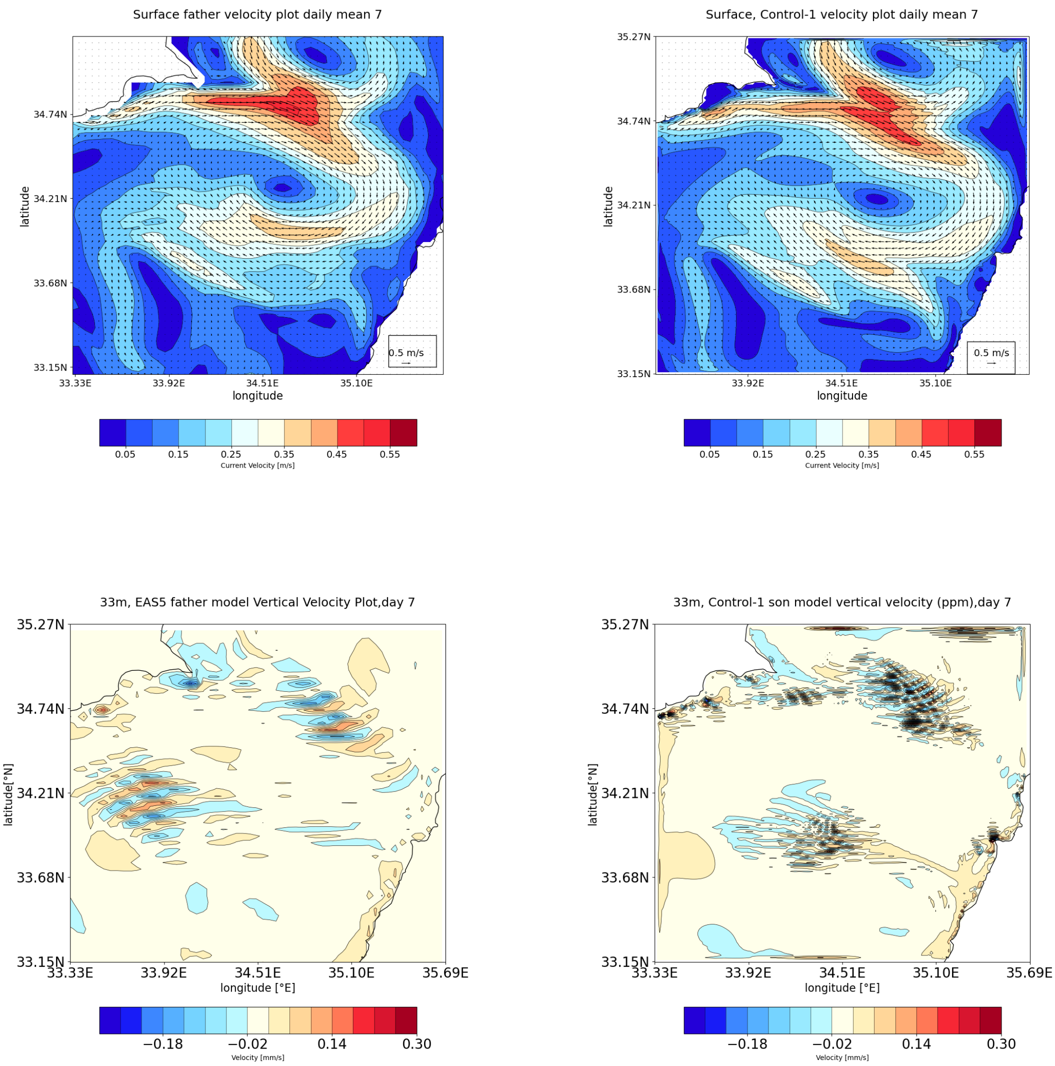

Figure 3.7: Top panel: 07/10/2020 surface, daily mean current velocity and amplitude plots of EAS5 (on the left) and Control experiment (on the right) Bottom panel: 07/10/2020 33m, daily mean vertical velocity plots of EAS5 (on the left) and Control experiment (on the right)

around 34.7 N and 34.5 E, where EAS5 reaches higher velocity peaks of over 0.5 m/s where Control-1 reaches inferior values aroun 0.45 m/s, this difference is very limited in the values and in the space, when in the rest of the domain the values are almost identical even if the current velocity amplitude is usually a little bit higher in EAS5 than in Control. This resemblance explains why the salinity fields are similar at the surface but not the differences observed in the temperature comparison, we can just state that these discordance is not caused from the temperature advection, but more likely from the Air-Sea fluxes.
The vertical velocities at 33m show great differences between the models, showing upwelling and downwelling current in different zones , resembling the differences between the Mixed Layers and explaining what previously observed in the temperature and in the salinity comparison. We can also notice that, as was predictable from the denser grid, the Control vertical velocity is much more uneven with a lot sharp peaks in delimited zones favouring the vertical mixing of the upper layers.

3.4.2 Air-Sea fluxes

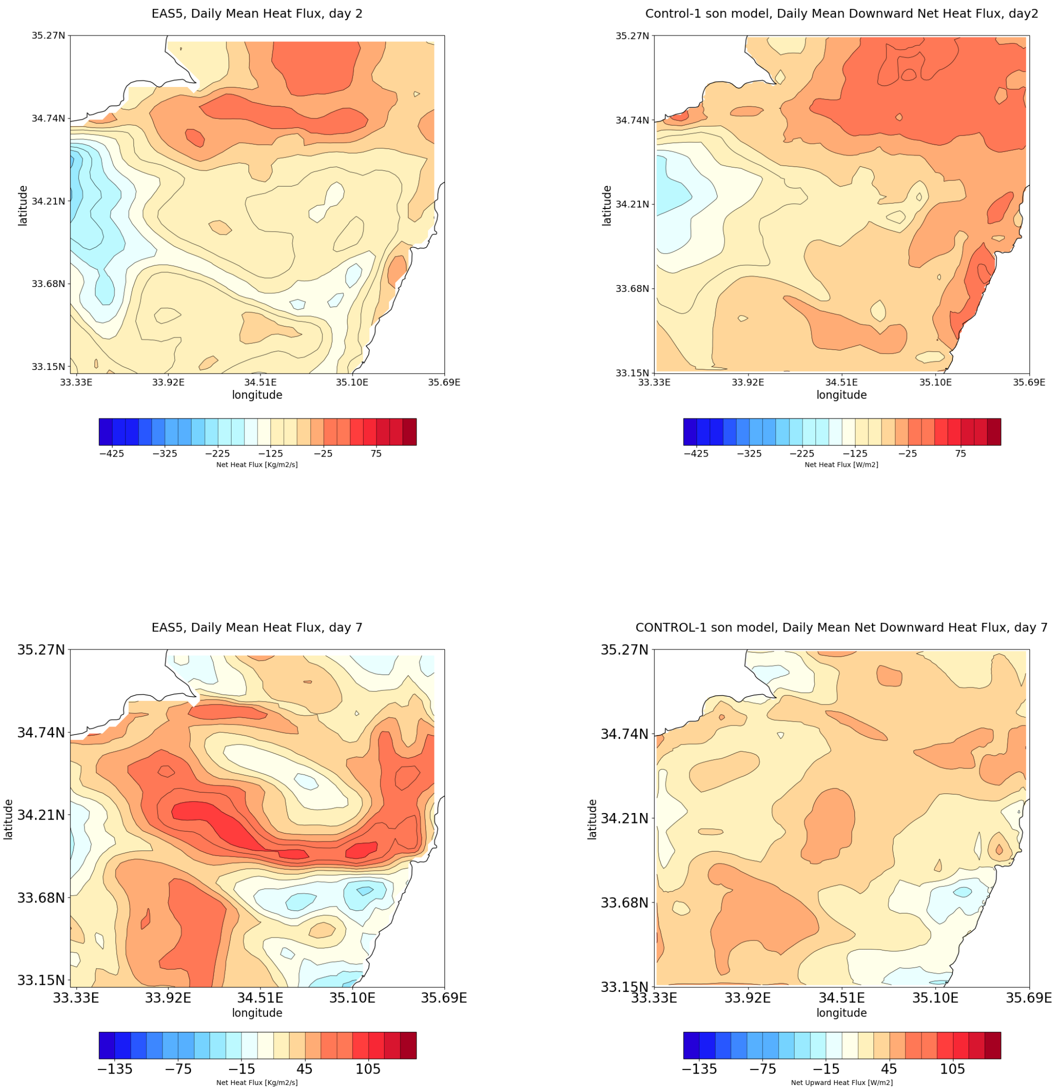

Figure 3.8: Top panels: Net Downward Heat Flux, daily mean on 02/10/2020, of EAS5 (on the left) and Control experiment (on the right)
Bottom panels: Net Downward Heat Flux, daily mean on 07/10/2020 of EAS5 (on the left) and Control experiment (on the right)

The Heat flux comparison shows important difference between the model and the experiment starting from the first days, with EAS5 that in the second day shows inferior Heat Fluxes values allover the domain with maxima just below 0 W/m^2 and minima under -250 W/m^2 and Control that goes from maxima around 20 W/m^2 to minima over the 225 W/m^2. In the seventh day the comparison resemble much of the temperature comparison, with EAS5 having a much uneven behavior with minima under -30 W/m^2 and maxima around 100 W/m^2 when Control shows minima about -15 W/m^2 and maxima around 75 W/m^2. IS important to notice how structurally after seven days the heat fluxes are extremely different with a much even distribution in the son model: this does not take place in the first days of run, resembling the behaviour of the Temperature field. Since the velocity and the salinity fields, as well as the water flux are not that different structurally neither intensity wise, there must be some process strictly correlated to the temperature, that slowly contributes to the horizontal mixing of the temperature. So we analyzed the temperature equation (eq.2.10) considering the consistency between the velocity fields we can argue that the advection cannot be responsible of this difference, the only remaining alternatives are D^T and F^T, thus the Air-Sea fluxes of the diffusion. To causally relate Heat Fluxes and Temperature is quite dubious since both influence each other evolution. As discussed in subsection 2.5.1 the two experiments have different formulation of the lateral diffusive and viscous operators, EAS5 has a not-eddy resolving formulation and Control has a eddy-resolving formulation. The eddy resolving formulation increases the overall horizontal diffusion and, since this small scale processes take time to exchange a significant amount of heat, it takes several days to change the horizontal structures of temperature field and Heat Flux.

3.5 Daily cycle and heat fluxes components

Finally we analyzed the daily cycles to verify the reliability of the model and the heat fluxes of the Control model, in preparation of further model comparisons.

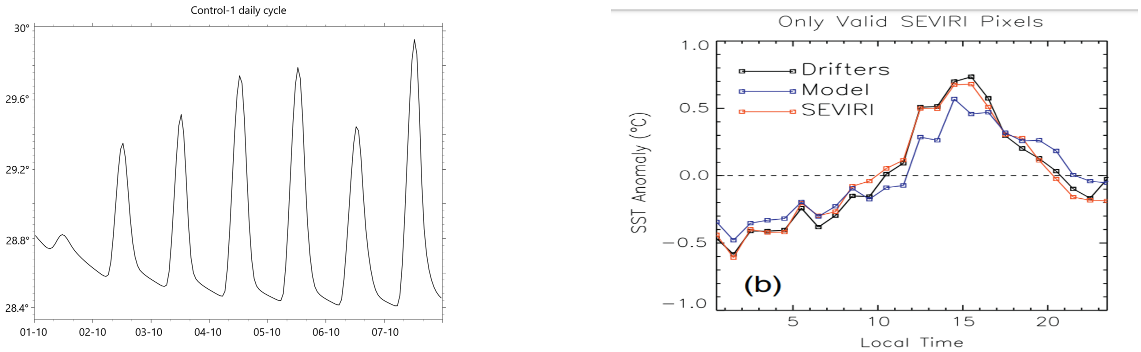

Figure 3.9:
Left panel: mean surface temperature over the domain, hourly means daily cycle from 01/10/2020 h 00:00 to 07/10/2020 h 23:00 of Control experiment.
Right panel: Mean SST anomalies obtained after removal of the mean daily value from mean hourly SST values from SEVIRI valid data (red), model (blue) and drifters (black) computed using all the satellite-in situ match-up points. Mean from day 160 to 240, 2011 in the Gulf of Lyons, as exposed in (Marullo et al., 2014)

The temperature daily cycle gives positives results, with a stable oscillation starting from the second day of forecasting with a maximal daily oscillation of about 1.5°C. We checked (Marullo et al., 2014), in particular Mean diurnal SST cycle measured and modeled in the Gulf of Lyons. Even if the period and the zone are not quite the same the consistency between the results is encouraging, increasing the reliability of the model. Also the minimum mean values around 28.4°C degrees and the maximum around 29.8°C are compatible with the documentation about this area in this part of the year (Ozsoy et al., 1981).

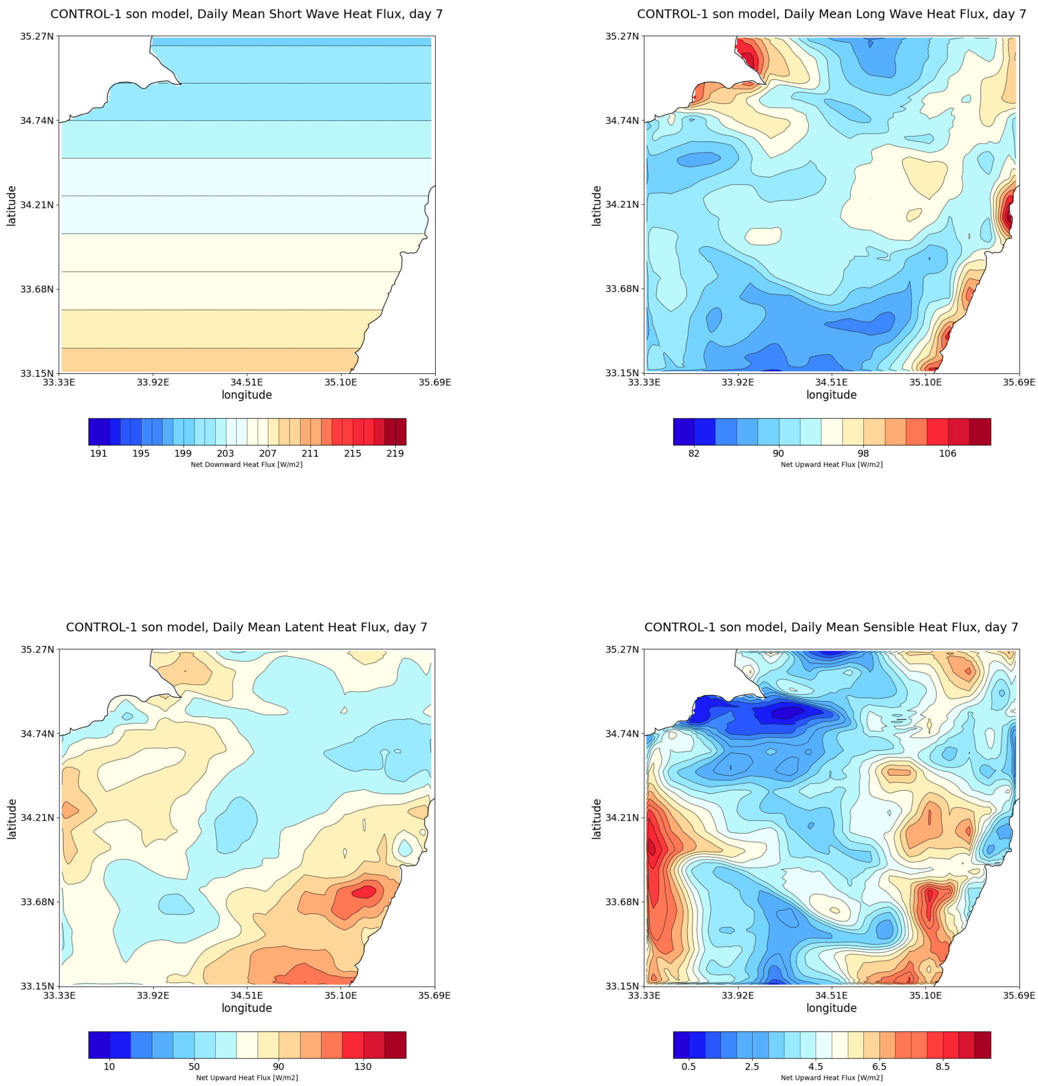

Figure 3.10: Control, daily mean heat flux components on 07/10/2020:
Top panel: Short Wave Heat Flux (on the left) and the Long Wave Heat Flux (on the right),
bottom panel: Latent Heat Flux (on the left) and Sensible Heat Flux (on the right).

In the Air-Sea Heat Fluxes component analysis we wanted to observe which processes dominate the net flux, not having the components of the father model wasn't possible to compare those, but they still allow us some considerations and hypothesis about the net heat flux comparison. Notice how the scale and the values of the Sensible Heat are one order of magnitude lower with respect to the other two, hence the Radiative and Latent components dominate the net heat flux, with the Sensible component almost neglectable. Because of his importance in the balance and the significant differences between the Air-Sea water fluxes, we can hypothesize that the latent heat flux probably will constitute an important discriminant between Control and the EAS5 net heat fluxes.

Chapter 4

Study cases of vertical mixing parameterization

In this chapter we focus on the vertical mixing parameterizations, in particular we wanted to compare the widely used Pacanowski-Philander, Richardson number dependent parameterization with the one equation Turbulent Kinetic Energy and the k-ϵ, GLS, two-equations closure. Since the father and the Control experiments use an enhanced diffusion convective parameterization we used the same for three experiments: TKE-1, GLS-1 and GLS-2. Then we removed it in the experiments TKE-2 and GLS-3 to reach an optimal choice of mixing parameterization. Following (Griffies et al., 2000), because of the presence of a less salty, colder Atlantic Waters we utilized a double diffusion scheme, that distinguish the computation of salinity diffusion coefficient of temperature and diffusion coefficient of temperature; the double diffusion convection should occur far from the Mixed Layer since Atlantic Waters are at about 100 m depth, as seen in Fig. 1.4, but the process can affect indirectly the Mixed Layer evolution.

For this reason experiments GLS-2 and GLS-3 used a double diffusion parameterization, in particular the comparison with the GLS-1 and the GLS-2 experiments results will show how this double diffusion process can be significant.

The GLS schemes used in particular a k-ϵ closure submodel, characterized by the following constants in the generic length scale equations (eq. 2.30 and 2.31, following (Rodi, 1987):

(p, n, m)	σ_k	σ_ω	C_1	C_2	C_3
(3, 1.5, -1)	1	1.3	1.44	1.92	1

4.1 Intercomparison between mixing parameterization schemes

We will consider first the experiments using the enhanced diffusion parameterization for the convection in all the mixing schemes; the simulations differ from Control experiment just in the vertical mixing parameterization, having the same domain, grid, period of interest, grid and other parameterizations:

Experiment name	**turbulence model**	**comments**
Control	Pacanowski-Philander with enhanced diffusion in the SML	meant to evaluate grid density effects
TKE-1	Turbulent Kinetic energy scheme with enhanced diffusion in the SML	meant to compare TKE and Pacanowski-Philander scheme effects
GLS-1	Generic Length Scale scheme (k-epsilon) with enhanced diffusion in the SML	meant to compare TKE and Pacanowski-Philander scheme effects
GLS-2	GLS (k-epsilon) with Double Diffusion and enhanced diffusion in the SML	meant to evaluate double diffusion effects

The comparison between the simulations with the measurements, will guide us in the understanding of an optimal vertical mixing parameterization.

In the considered domain we have two ARGO floats, each one collected two in-situ temperature and salinity profiles in our period of interest. Hence we have four profiles for each tracer, each ARGO profile location and data collecting period follows:

product name	**location**	**time**
GL_PR_PF_6903269_20201001	P_01: (34.44 N, 34.10 E)	01/10/2020 h 06.00
GL_PR_PF_6903269_20201006	P_06: (34.46 N, 34.18 E)	06/10/2020 h 06.00
GL_PR_PF_6903786_20201002	P_02: (33.36 N, 34.84 E)	02/10/2020 h 21.00
GL_PR_PF_6903786_20201007	P_07: (33.39 N, 34.82 E)	07/10/2020 h 21.00

Since we considered the day 01/10/2020 as a spin-up day for our experiments we disregarded both temperature and salinity profiles that day.

To understand the effect of enhanced diffusion on our schemes it has been necessary to carry out a comparison of the diffusivity profiles.
Each vertical comparison was made in correspondence of an ARGO data profile, to also gain an better physical interpretation of our results.

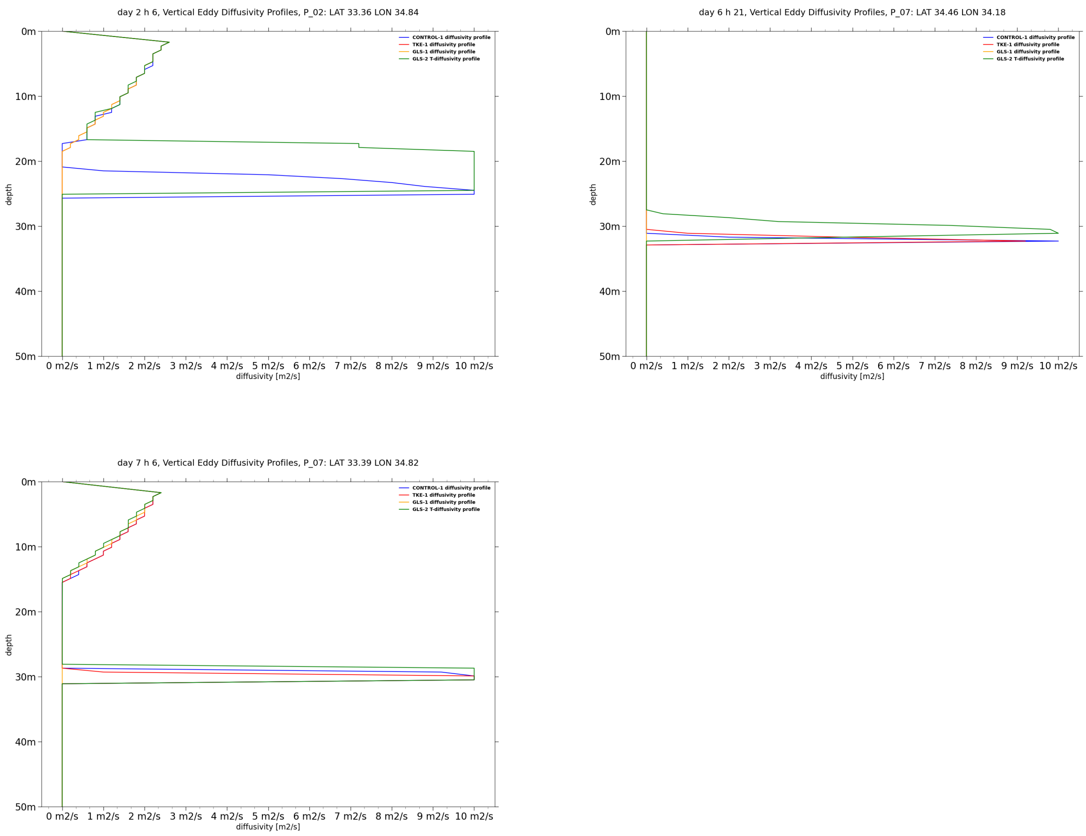

Figure 4.1: Vertical diffusivity profiles, hourly means of Control, TKE-1, GLS-1 and GLS-2 experiments.
Top left panel: point P_02 day 02/10/2020 h 06.00
Top right panel: point P_06 day 06/10/2020 h 21.00
Bottom panel: point P_02 day 07/10/2020 h 06.00

In each comparison in Fig. 4.1 we can observe how the diffusivity peaks at the bottom of the mixed layer. Knowing that enhanced diffusion brings a default value of

10 m^2/s in the presence of gravitational instability, these peaks are easily explainable. In the transition zone between the mixed layer and the lower layers we have high gradients of temperature and salinity, this will likely cause gravitational instability (N^2 gets negative values) and consequently the enhanced diffusion is activated. What is less explainable are the staircase in the first 15 meters in P_02 and P_07 profiles. An hypothesis can be the numerical instability of our experiments, although considering the proximity of the locations of the two profiles and observing how the peak of the staircase reduced from 2.7 m^2/s to about 2.4 m^2/s and how the base of the staircase reached 20 m depth at the second day and about 15 m at the seventh we can conclude that this structure is getting weaker as the time progresses. Since these have no physical interpretation will be interesting to compare them with the diffusivity profiles of the experiments without the enhanced diffusion, to understand if it's a flaw of this parameterization or a more general numerical stability problem.
Is also relevant that the GLS-2 experiment diffusivity reach higher values than the other schemes in all the comparisons, we can hence suppose a stronger mixing with respect to the other schemes.

4.1.1 Tracers comparison

We compare now the tracers fields of the TKE-1, GLS-1 and GLS-2 experiments with the Control experiment; in particular the Surface horizontal fields and the 33 m fields again to compare how the experiments behave at the surface and at the bottom of the mixed layer. To highlight the disagreements between the models we plotted the differences between the fields.

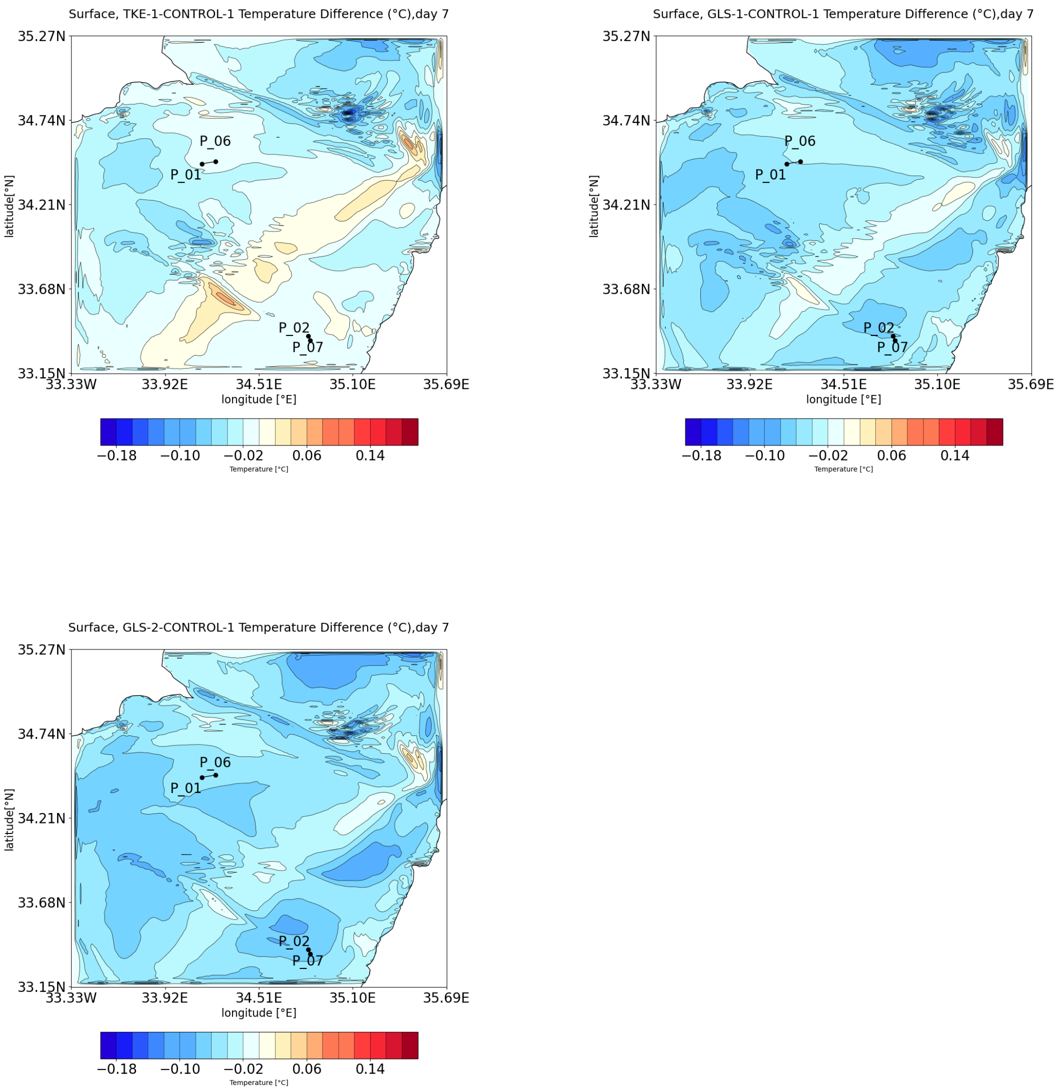

Figure 4.2: Surface temperature difference between TKE-1 experiment and Control (in the top left panel), between GLS-1 experiment and Control (in the top right panel) and between GLS-2 experiment and Control (in the bottom panel), daily mean on 07/10/2020.

The surface temperature comparison shows how GLS-1 and GLS-2 experiments develop lesser values than the Control experiment; in particular the GLS-2 experiment after seven days develops a difference of about -0.1° C with peaks of -0.15° C.

The GLS-1 experiment has a similar behaviour but is a little warmer: after seven days develops a difference of about 0.05° C with peaks of 0.1° C.
TKE-1 comparison is more ambiguous, showing often lower temperatures but also locally warmer structures as happens for instance around 33.7° N, 34.3° E, with a peak of about 0.8°. We can also notice that all the three comparisons and in particular the GLS-1 and GLS-2 comparisons show similar structures, due to the resemblance of the vertical parameterizations (both TKE and GLS closures are based on the Turbulent Kinetic Energy equations)

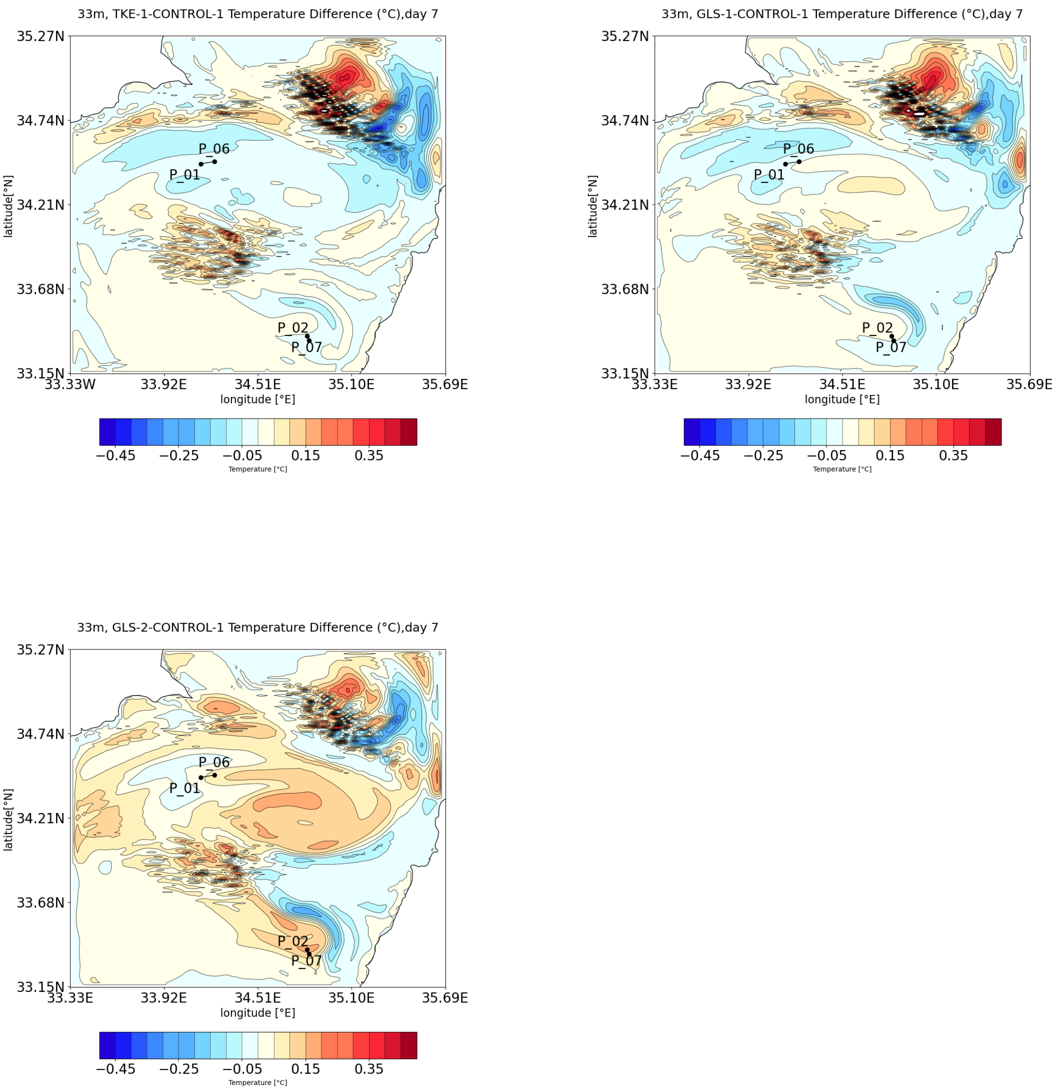

Figure 4.3: temperature difference at 33 m depth between TKE-1 experiment and Control (in the top left panel), between GLS-1 experiment and Control (in the top right panel) and between GLS-2 experiment and Control (in the bottom panel), daily mean on 07/10/2020.

The 33m depth comparison shows how the mixed layer base of TKE-1, GLS-1 and GLS-2 develops differently than the Control experiment one: in particular we observe great differences in the region between 34.2 N and 35.2 N and 34.7 E and 35.7 E. Here TKE-1 and GLS-1, that are very similar at this depth, develop positive and negative differences with peaks of almost 0.5°, developing a deeper ML in the North-Western part of the region and a thinner one in the South-Eastern part. GLS-2 shows a similar behaviour but with reduced differences, furthermore this experiments shows higher temperatures, of about 0.1°-0.15° in a wide part of the domain, differently from the other experiments that don't have such significant differences.

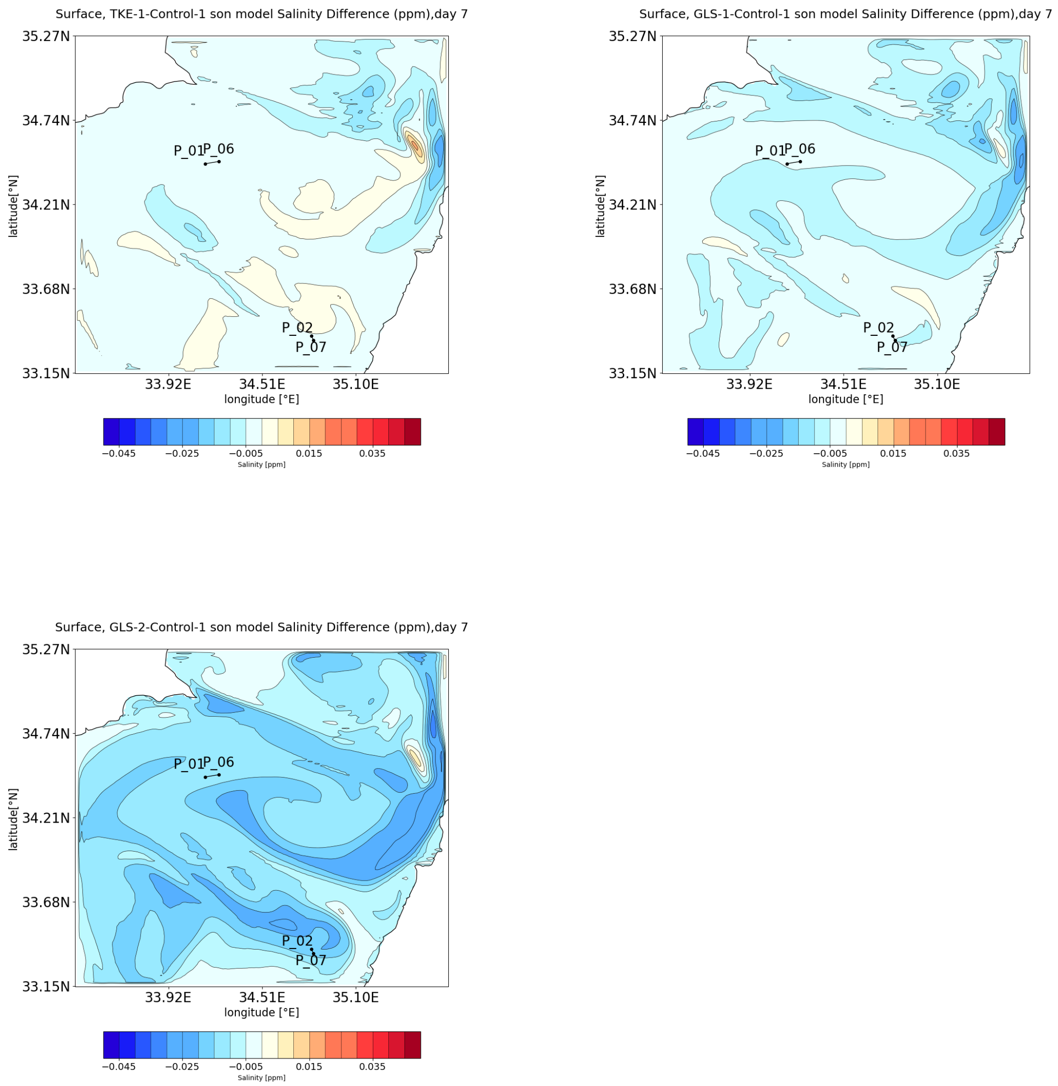

Figure 4.4: Surface salinity difference between TKE-1 experiment and Control (in the top left panel), between GLS-1 experiment and Control (in the top right panel) and between GLS-2 experiment and Control (in the bottom panel), daily mean on 07/10/2020.

The surface salinity comparison shows how GLS-1 and GLS-2 experiments develop lesser values than the Control experiment; in particular the GLS-2 experiment after seven days develops a difference of about -0.02 PSU with peaks of -0.035 PSU.

The GLS-1 experiment has a similar behaviour with similar structures but smaller differences: after seven days develops a difference of about -0.01 PSU with peaks of -0.3 PSU.
TKE-1 has a similar behaviour but with different structures and even smaller differences: after seven days develops a difference of about -0.005 PSU, not particularly significant, with peaks of -0.25 PSU.

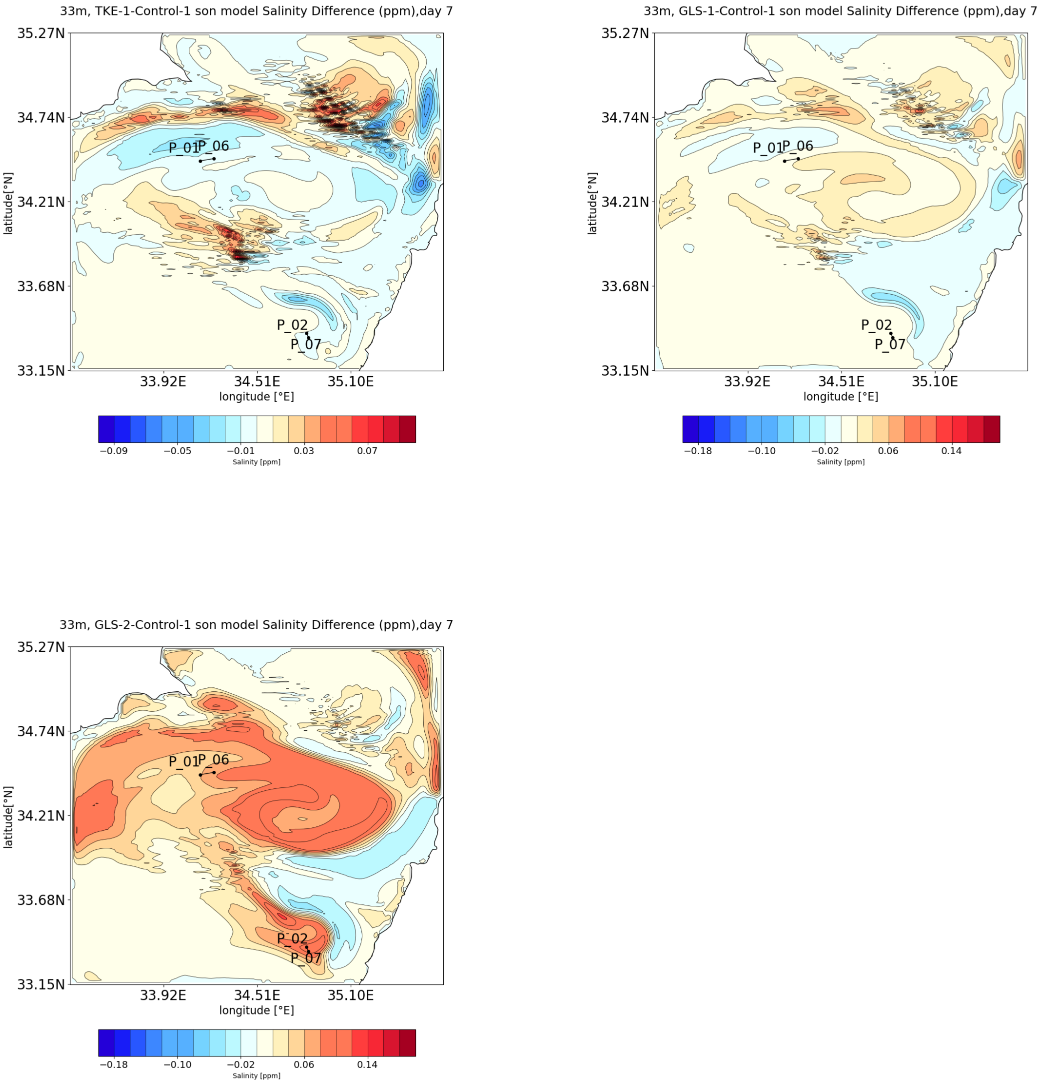

Figure 4.5: Salinity difference at 33 m depth between TKE-1 experiment and Control (in the top left panel), between GLS-1 experiment and Control (in the top right panel) and between GLS-2 experiment and Control (in the bottom panel), daily mean on 07/10/2020.

In the 33 m depth salinity comparison the three experiment behave differently: The TKE-1 experiment like in the temperature comparison shows great differences in the region between 34.2 N and 35.2 N and 34.7 E and 35.7 E, with a higher salinity

in the north-west of the region an lower salinity in the south-east with posivite and negative peaks of almost -0.1 PSU, probably caused from a different development of the Mixed Layer, deeper in the NW and thinner in the SW; in general TKE-1 doesn't show a dominant behaviour, with positive and negative differences distributed over the domain.
GLS-1 doesn't develop the same structures seen in the temperature comparison, showing that the temperature an the salinity behave differently at this depths as we will see also in the vertical profile; furthermore GLS-1 seems to develop higher values than Control with peaks of 0.1 PSU in the salinity difference.
GLS-2 difference with Control resembles the structure seen in GLS-1 comparison but with more significative differences, with a 0.06 PSU higher salinity for most of the domain and peaks of about 0.12 PSU.

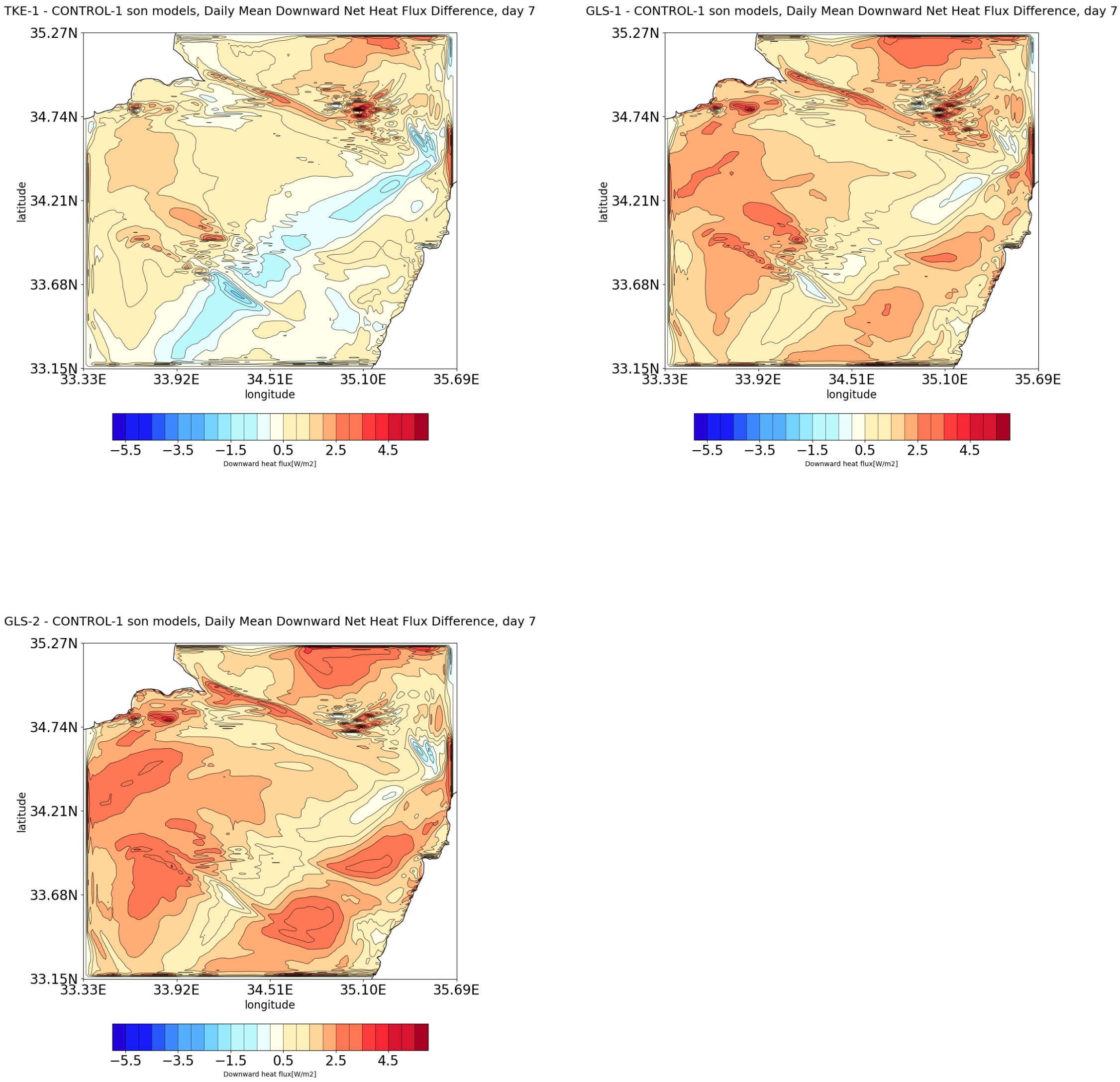

Figure 4.6: Net Downward Heat Flux difference, daily mean day 7/10/2020, between TKE-1 and Control (left panel), between GLS-1 and Control (top right panel) and between GLS-2 and Control (bottom panel).

The Net Downward Heat Flux comparison mirrors what was observed in the temperature comparison:
TKE-1 has a stronger downward heat flux of about 1-1.5 W/m^2 in most of the domain, with some exceptions, mainly around 33.7° N, 34.3° E, with a peak of -2.5 W/m^2 in

the Heat flux difference with Control experiment. GLS-1 shows a stronger heat flux of about 1.5-2 W/m^2 for most of the domain, with positive peaks of about 3 W/m^2 in the difference with Control experiment. GLS-2 resembles GLS-1 behaviour with a stronger heat flux of about 2-2.5 W/m^2 in most of the domain with respect to Control with peaks up to 4 W/m^2
The interpretation of these heat fluxes comparison is quite obvious, where the experiments developed a lower daily surface temperature, with respect to Control experiment, the downward heat flux was stronger, proportionally to the temperature difference, at the contrary where the temperature difference with Control was positive they developed a weaker heat flux. This is due to the dependency of the Latent, Sensible and Long Wave components on the superficial temperature, as the temperature rises, these components grow and, since they have a negative contribute to the Net Downward Heat Flux (as seen in equation 2.14) cause an energy loss in the total budget. At the contrary with lower temperature we have weaker Latent, Sensible and Long Wave heat components and a gain in the Net Downward Heat Flux.

The comparison with in situ measurements is essential for experiments evaluation, obviously the limited availability of observational information doesn't allow us to get strong statements, but will guide several choices and further considerations over our experiments. Although we have four profiles for each tracer, as descripted in Table 4.1, however we utilized just three of them because the one of the available data is taken in the fist day of forecasting, that the Control daily cycle showed as a spin-up day, therefore the experiments are not reliable and cannot be compared.

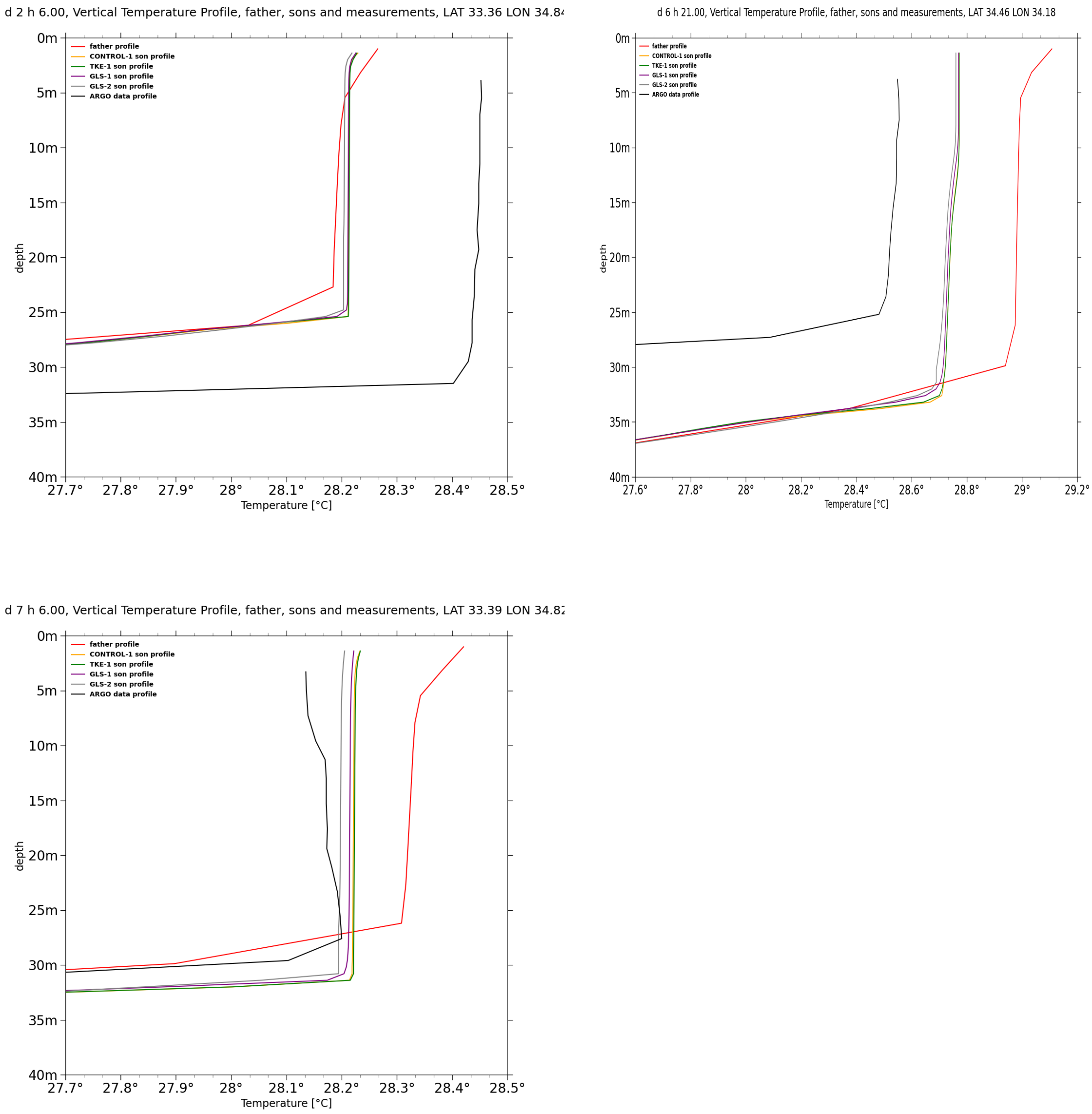

Figure 4.7: Vertical hourly mean temperature profiles, ARGO observations, EAS5, TKE-1, GLS-1 and GLS-2 predictions.
Top left panel: point P_{02} day 2/10/2020, h 06.00.
Top right panel: point P_{06} day 6/10/2020, h 21.00,
Bottom panel: point P_{07} day 7/10/2020, h 06.00

The temperature comparison show how each experiment: Control (in yellow), TKE-1 (green), GLS-1 (purple) and GLS-2 (grey) better resemble the observations (black)

of the mixed layer, with respect to EAS5 model (red), this tells us that the downscaling affects positively our experiments, improving the temperature field.
Can also be noticed how in two occasions (in the sixth and the seventh day comparison) the model GLS-2 performs significantly better than the other experiments, in the second day on the contrary the differences are less significant. We can also notice how in all the cases the experiments develop a deeper mixed layer with respect to EAS5, and in two cases of the ARGO profiles; is also conforting to observe how the mixed layer base is in the same location of the peaks of the diffusion: at about 28m depth in the second day, at about 35m depth in sixth and at about 32m depth in the seventh, this gives further reliability to our models. Finally we can observe how the TKE-1 and the Control experiments are essentially indistinguishable from each other in all the comparison, meaning that, as far as concerns the temperature, the TKE closure doesn't bring any improvement over the Pacanowski-Philander. Differently GLS-1 shows little improvements with respect to the Control experiments in the sixth and in the seventh day, being practically equal in the other case.

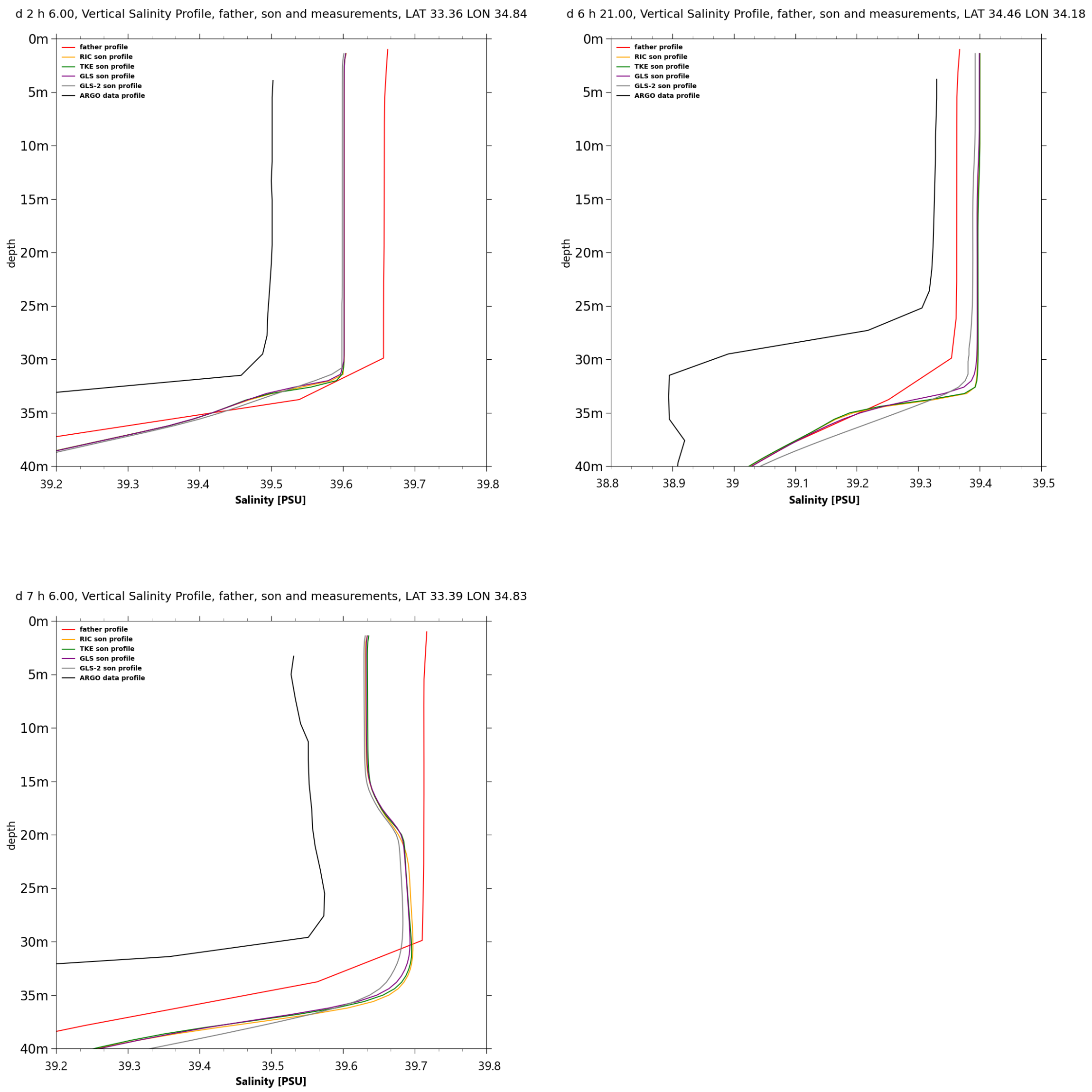

Figure 4.8: Vertical hourly mean salinity profiles, ARGO observations, EAS5, TKE-1, GLS-1 and GLS-2 predictions.
Top left panel: point P_{02} day 2/10/2020, h 06.00.
Top right panel: point P_{06} day 6/10/2020, h 21.00, Bottom panel: point P_{07} day 7/10/2020, h 06.00

The salinity comparison is more ambiguous than the temperature one, in order to establish a better behaviour of the experiments with respect to EAS5, since the P_2

and the P_7 comparisons confirm in the salinity what observed about the temperature but the P_06 comparison show the opposite. This states that the positive effect of the downscaling is not an absolute truth and there are several exceptions to be taken account of.
The comparison between experiments shows first of all an high similarity:
Control, TKE-1 and GLS-1 are practically indistinguishable in all the comparisons, differently GLS-2 that shows a better behaviour in the seventh and, especially in the sixth day, confirming his better modelling of the Mixed Layer.

From the comparison between the experiments we can conclude that the GLS (k-/*epsilon*) vertical parameterization brings a stronger mixing, lowering the superficial temperatures and salinity and increasing them at the base of the mixed layer, this causes also a stronger Net Downward Heat Flux. The presence of a double diffusion parameterization increases these phenomena as we could observe in the comparison between GLS-1 and GLS-2.
The comparison with the in situ observations establish that the downscaling has positive effects in the modelling of the mixed layer, with an exception in the salinity comparison. Furthermore the observation show how the different behaviour of GLS-1 and especially GLS-2 brings a better resemblance of observational data, both in terms of Temperature and Salinity. Finally the comparison between TKE-1 and the Control experiment shows not many significant differences in the horizontal comparison and a indistinguishable behavior with respect to the in situ observations. Is interesting how a finer Turbulent Kinetic Energy dependent parameterization perform similar to a Richardson Number Dependent closure submodel but we must remember that the choice of the enhanced diffusion parameterization of the convection is suboptimal (or even rough) for the TKE and the k-ϵ closure submodels.

4.2 Optimal vertical mixing parameterization

The TKE and GLS turbulent closure schemes presented in section 2.6 deal, in theory, with statically unstable density profiles. In such a case, the term corresponding to the destruction of turbulent kinetic energy through stratification in equation 2.21 or equation 2.31 becomes a source term, since N^2 is negative. It results in large values of the viscosity and diffusivity coefficients. These large values restore the static stability of the water column in a way similar to the enhanced vertical diffusion parameterization (subsection 2.6.5). However, in the vicinity of the sea surface (first ocean layer), differently from the enhanced diffusion scheme, the eddy coefficients computed by the turbulent closure scheme do not usually exceed 10^{-2} m^2/s, because the mixing length scale is bounded by the distance to the sea surface. These values are much more physical than the 10 m^2/s assumed for the enhanced diffusion, hence we remove the enhanced diffusion parameterization in two experiments described in Table 4.1 In the domain, grid, period of interest, time step and all the other parameterizations, the experiments are identical to the previous TKE-1, GLS-1 and GLS-2 and to the Control experiment.

Experiment name	**turbulence model**	**comments**
TKE-2	Turbulent Kinetic energy submodel	meant to compare TKE and Pacanowski-Philander scheme effects without the enhance diffusion contribution
GLS-3	GLS (k-epsilon) submodel with Double Diffusion	meant to test how the most effective turbulent closure behave without the enhance diffusion contribution

Table 4.1

4.2.1 Comparison between the experiments

Since the discriminant between these models and the previous stays in the diffusivity parameterization, we started from that comparing Control and the two experiments.

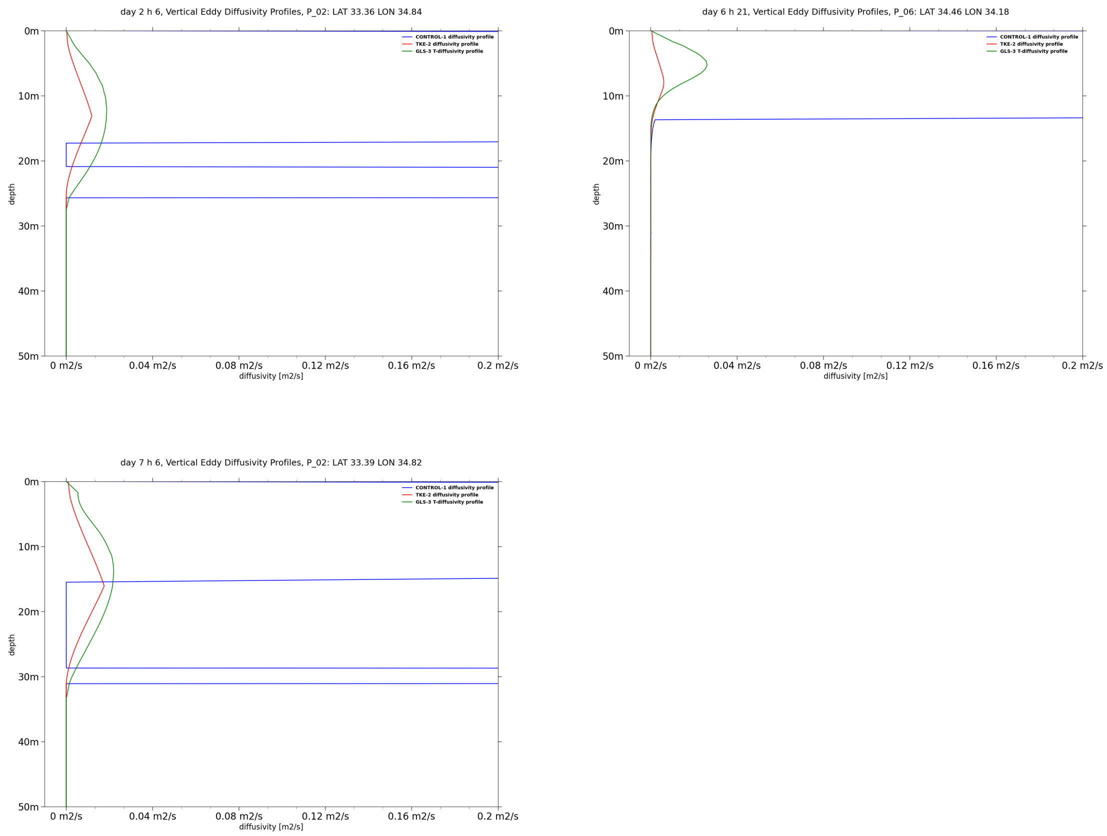

Figure 4.9: Vertical diffusivity profiles, hourly means of Control, TKE-2 and GLS-3 experiments.
Top left panel: point P_{02} day 02/10/2020 h 06.00
Top right panel: point P_{06} day 06/10/2020 h 21.00
Bottom panel: point P_{07} day 07/10/2020 h 06.00

In Figure 4.9 we can note how the diffusivity of GLS-3 and TKE-2 is about three order of magnitude lower than the enhance diffusion peaks seen in the previous experiments, with highest values under 0.04 m^2/s, against the 10 m^2/s of the enhanced diffusion parameterization . However out of the vertical unstable zones, the two models have diffusivity values much higher than Control, this producing a more uniform diffusivity profile. We can also notice the dependency of the diffusivity to the mixing length, and hence to the depth in the first 5-10 meters, especially in the linear growing of TKE-2 diffusivity in that zone. Finally we can also notice that GLS-3 always shows higher diffusivity values of TKE-2 with much smoother, physical profiles.

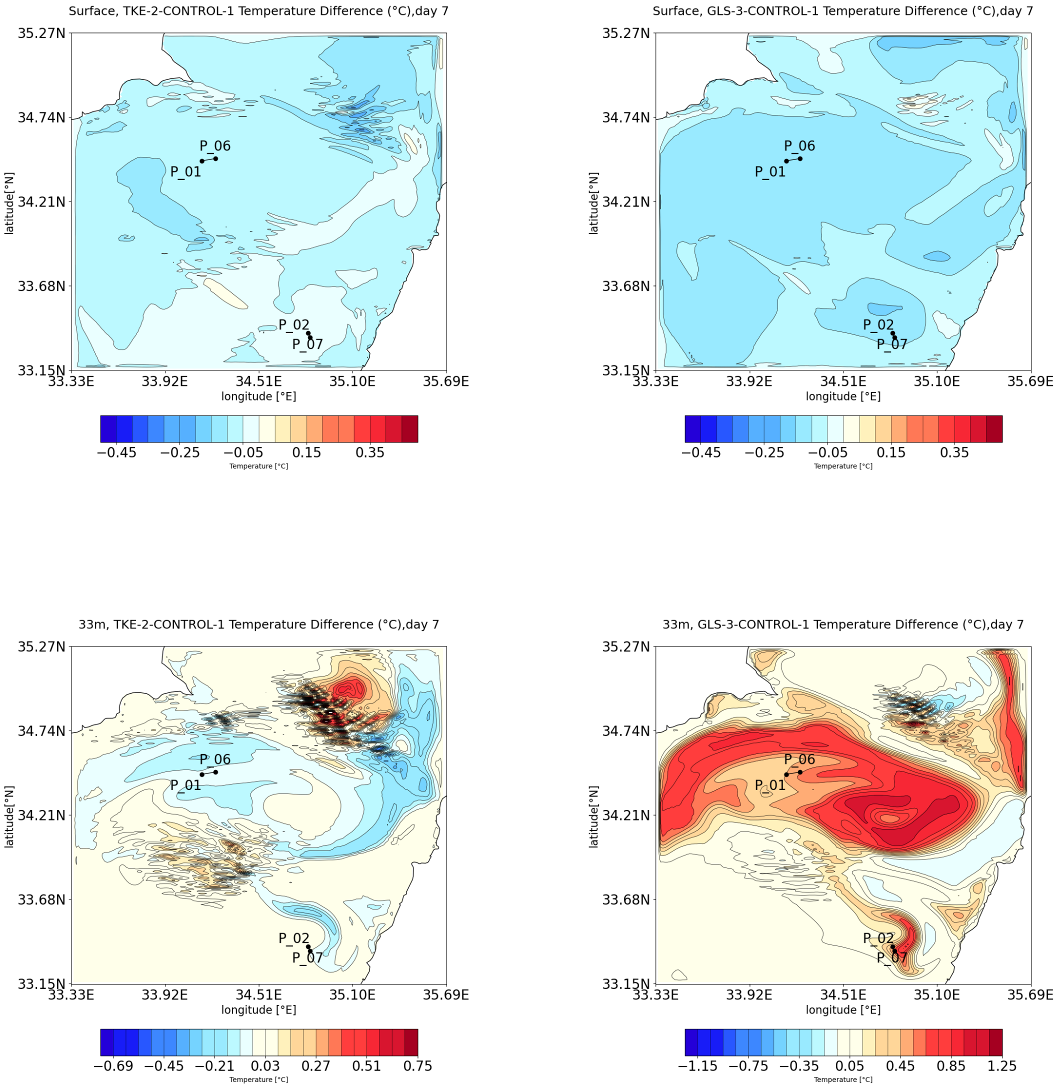

Figure 4.10: Top panels: Surface temperature difference between TKE-2 experiment and Control (in the left panel) and between GLS-3 experiment and Control (in the right panel), daily mean on 07/10/2020.
Bottom panel : temperature difference at 33 m depth between TKE-2 experiment and Control (in the left panel)and between GLS-3 experiment and Control (in the right panel), daily mean on 07/10/2020.

The surface temperature comparison in Fig. 4.10 gives for GLS-3 experiment, similar

results with respect to his corresponding GLS-2. As shown before TKE-2 gives different results with respect to the TKE-1 experiment, especially in the surface temperature: TKE-2 surface temperature difference with Control shows a significantly lower values, having a 0.05°-0.1° C lower temperature in most of the domain with peaks of about -0.25°C. At 33 m the temperature is very different, with a temperature between 0.6° C and 1° C warmer than Control in most of the domain. This is the largest difference between Control and the study cases that we have carried out and we will see later that this is an improvement with respect to observations.
The GLS-3 surface temperature difference with Control shows even lower temperatures, having a 0.1°-0.15° C inferior temperature in most of the domain with respect to Control with peaks of over -0.25°C. In the 33 m comparison it shows a similar temperature about half the domain, with great temperature differences, about 0.6° C with peaks of over 1°C in the other half.

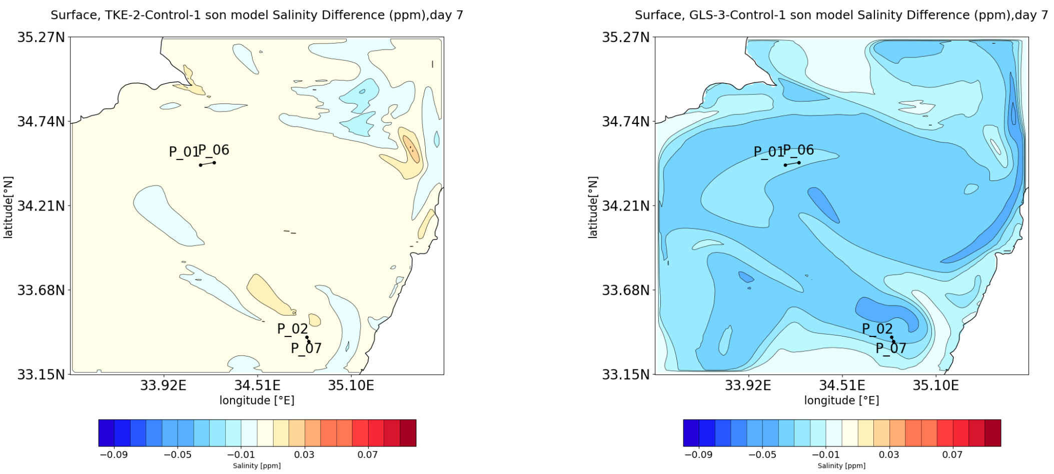

Figure 4.11: Surface salinity difference between TKE-2 experiment and Control (in the left panel) and between GLS-3 experiment and Control (in the right panel), daily mean on 07/10/2020.

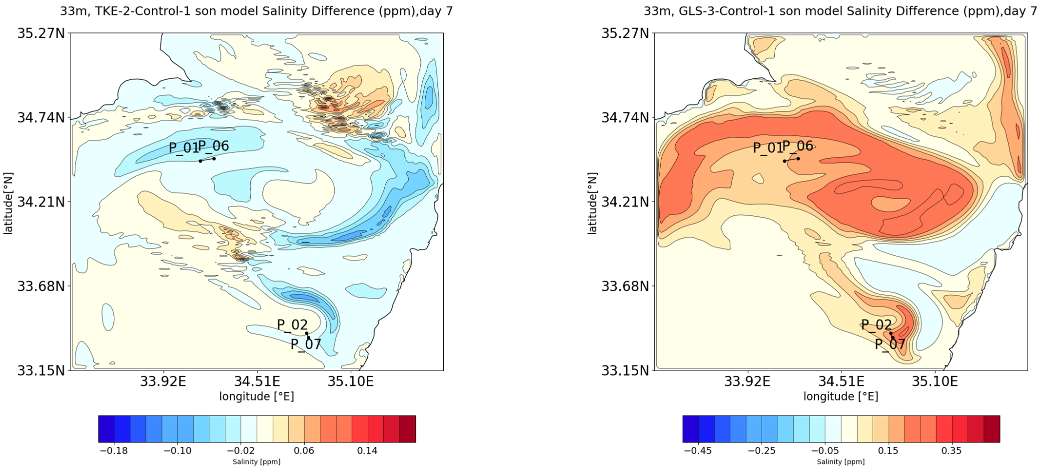

Figure 4.12: Salinity difference at 33 m depth between TKE-2 experiment and Control (in the left panel) and between GLS-3 experiment and Control (in the right panel), daily mean on 07/10/2020.

The salinity comparison gives continuity to the results of the temperature as far as concerns the GLS-3 experiment, however it shows that TKE-2 behaves similarly to Control and TKE-1 experiments. TKE-2 surface salinity difference with Control shows a similar values, having differences under 0.01 PSU in most of the domain. In the difference at 33 m depth it shows again similar values with respect to Control in most of the domain, with differences mostly under 0.02 PSU, with the exception of positives and negative peaks of about 0.08 PSU in structures analogous of what observed in the temperature comparison and in the TKE-1 salinity comparison.
The GLS-3 surface salinity difference with Control shows GLS-3 having lower values, with a 0.03-0.04 psu inferior salinity in most of the domain with respect to Control with peaks of over 0.05 PSU. In the 33 m comparison, as happened for the temperature it shows a similar salinity in about half the domain, with great differences, about 0.1 PSU with peaks of over 0.2 PSU in the other half.

The key element for the evaluation of TKE-2 and GLS-3 is the comparison with in situ measurements, in our case the Temperature and Salinity ARGO profiles. The latter have been compared not only to the TKE-2 and GLS-3 but also to the previous TKE-1 and GLS-2.

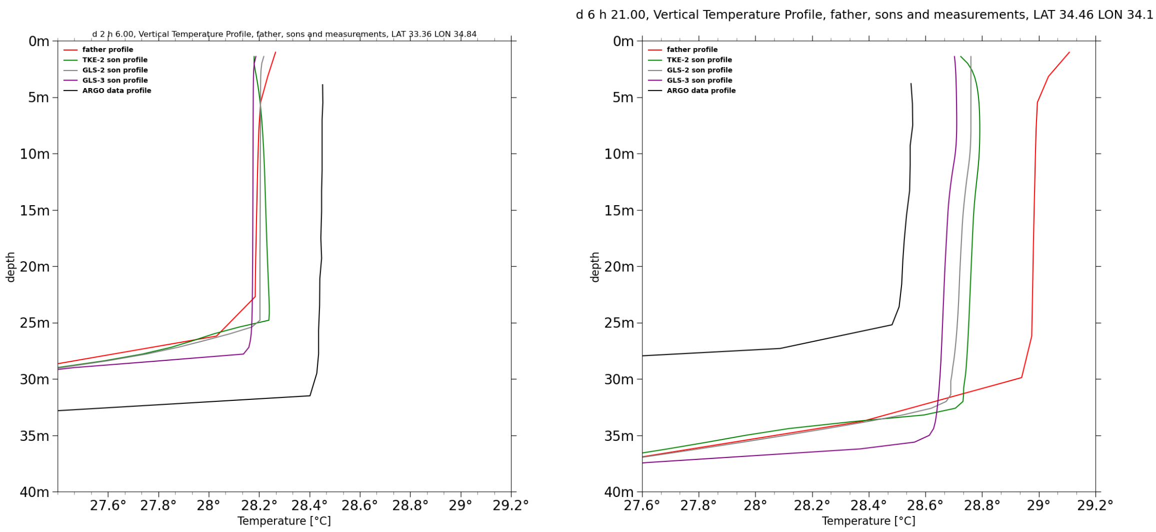

y ev

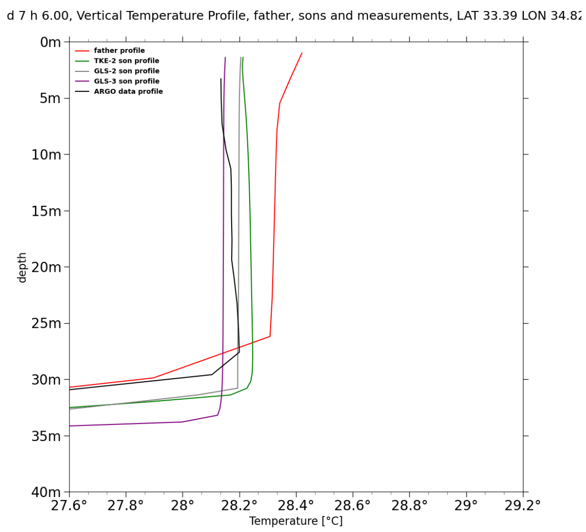

Figure 4.13: Vertical hourly mean temperature profiles, ARGO observations, EAS5, TKE-2, GLS-2 and GLS-3 predictions.
Top left panel: point P_{02} day 2/10/2020, h 06.00.
Top right panel: point P_{06} day 6/10/2020, h 21.00, Bottom panel: point P_{07} day 7/10/2020, h 06.00

In the temperature comparisons, Fig. 4.13, we observe that GLS-3 is closest to ARGO profiles for values of mixed layer temperature. TKE-2 performs significantly worse than the two GLS experiments and, in two cases, showing a significantly decreasing temperature, about 0.1°, in the fist five meters, probably indicating a problems in the resolving of vertical gravitational instabilities in the upper layers; this is often due to the mixing length depending from the depth, near the surface the mixing length is low and, for this reason, the diffusivity can't grow enough despite the negative sign of N^2 create a source term in the TKE equation. For this reason we can conclude that the enhance diffusion parameterization makes, sense also in case of a Turbulent Kinetic Energy vertical parameterization, helping to resolve these gravitational instabilities. About the mixed layer depth we can observe how the TKE has a thermocline comparable with GLS-2 and the previous experiment, however GLS-3 develops a deeper thermocline in all the cases, which however is not closer to the observed profile. Thus it seems that for the temperature, the mixed layer is not well parameterized by the GLS-3 scheme and more work will be needed to limit the diffusion, probably with a better modeling of the upward advection of the temperature.

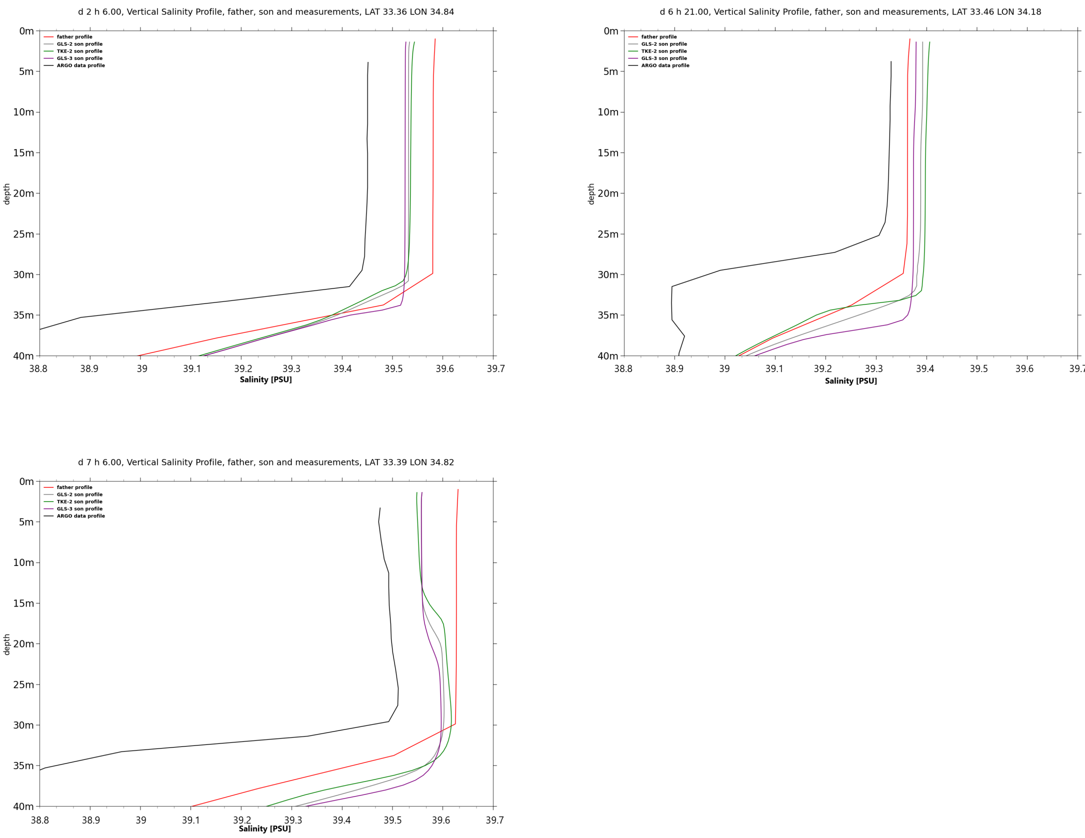

Figure 4.14: Vertical hourly mean salinity profiles, ARGO observations, EAS5, TKE-2, GLS-2 and GLS-3 predictions.
Top left panel: point P_{02} day 2/10/2020, h 06.00.
Top right panel: point P_{06} day 6/10/2020, h 21.00,
Bottom panel: point P_{07} day 7/10/2020, h 06.00

For the salinity GLS-3 consistently gives slightly better results than the GLS-2, confirming how the enhanced diffusion is unnecessary and even counterproductive in this case, on the contrary the vertical salinity profiles of TKE-2 doesn't seem to compensate the vertical temperature gradient at the surface confirming the vertical instability in the TKE-2 profiles and probably the necessity of an enhanced vertical diffusion parameterization in that case. Again we can note that TKE-2 halocline is comparable with GLS-2 and TKE-1, on the contrary GLS-3 has always deeper haloclines, confirming the deepening of the mixed layer and the increase of the vertical mixing.
The important difference between the mixed layer depth between experiments and observations can be explained taking account of the processes that contribute to its formation. On one hand we have the vertical downward diffusion, that deepens the

ML warming under his base, on the other hand we have the upward advection of the temperature, that brings up deeper, cooler water, reducing the MLD. Our hypothesis is that, since our experiments don't resolve the submesoscale, they ignore several upwelling processes that would bring a cooling of the mixed layer base keeping it shallower.

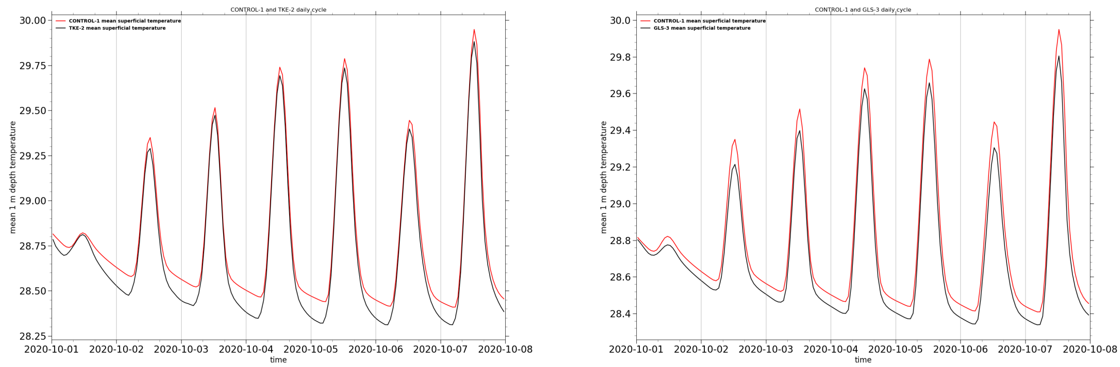

Figure 4.15: Left panel: mean surface temperature over the domain, hourly means daily cycle from 01/10/2020 h 00:00 to 07/10/2020 h 23:00 of Control and TKE-2 (left panel) and GLS-3 experiment (right panel)

It is interesting to compare the daily cycles between different experiments, this us a point of view on the different evolution of the experiments as the time progresses, such comparison is shown in Fig. 4.15
TKE-2 shows comparable warm peaks to Control while the lower temperatures are significantly cooler with respect to Control, this behaviour results in a higher amplitude of the daily cycle. Since the heat fluxes are comparable even if a little stronger, we can hypothesize that the previously observed mixing problem near the ocean surface (due to the mixing length dependence on the depth) brings the lower ocean layers to be less affected by the temperature daily cycles, decreasing the mass and hence the heat capacity of the water involved in the process, therefore increasing the oscillations between diurnal and nocturnal temperatures.
GLS-3 is consistently cooler than Control over the time, with highest hourly mean temperature over the domain of about 29.6°C and lowest of about 28.4° C.
Is quite interesting to notice how the temperature gaps between the experiments mean temperature is formed in the spin up day and than remains quite constant for GLS-3 while oscillates for TKE-2 between days and nights as previously noticed, this means that the difference in the mean temperatures, differently from the differences in the

structures, is not significantly evolving over the time, but is almost entirely determined in the experiment initialization.

As for the previous cases we compared the heat fluxes with the Control experiments, showing how the temperature difference at the surface affect the transfer of heat, moreover we compared the single components of the heat balance to understand which processes determine the differences in the net balance. The conclusions were quite aligned with what observed in subsection 3.4.2 about the weight of each heat flux component in the total balance apart of the Shortwave Radiation Heat flux, that obviously doesn't show significant differences.

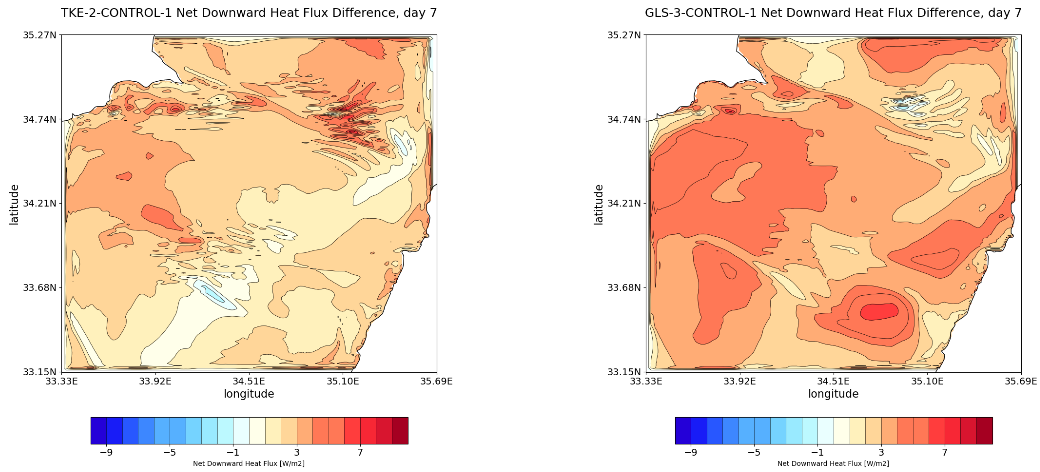

Figure 4.16: Net Downward Heat Flux difference, daily mean day 7/10/2020, between TKE-2 and Control (left panel) and between GLS-3 and Control (right panel).

The net downward heat flux comparison shown in Fig. 4.16 predictably resembles what stated in the horizontal comparison of the surface temperature, also the observations made in the temperature daily cycle comparison are in agreement with the trend of the Net Heat Fluxes differences between the two experiments and Control:
TKE-2 shows a different behavior with respect to what observed for TKE-1 in subsection 4.1.1, having a stronger downward heat flux of about 2-3 W/m^2 in most of the domain, with some exceptions, mainly around 33.7° N, 34.3° E, with a peak of -2.5 W/m^2 in the Heat flux difference with Control experiment. Hence TKE-2 Downward Net Neat Heat Flux is more intense with respect to the TKE-1 experiment, that is

not surprising considering the lower surface temperatures.

GLS-3 has a stronger heat flux of about 3-4 W/m^2 in most of the domain with wide part having values of over 4 W/m^2, hence considering again what observed in subsection 4.1.1 his is the stronger net heat flux of the considered models in accordance with his lowest surface temperatures pointed out in subsection 4.2.1 and also in the previous daily cycle comparison.

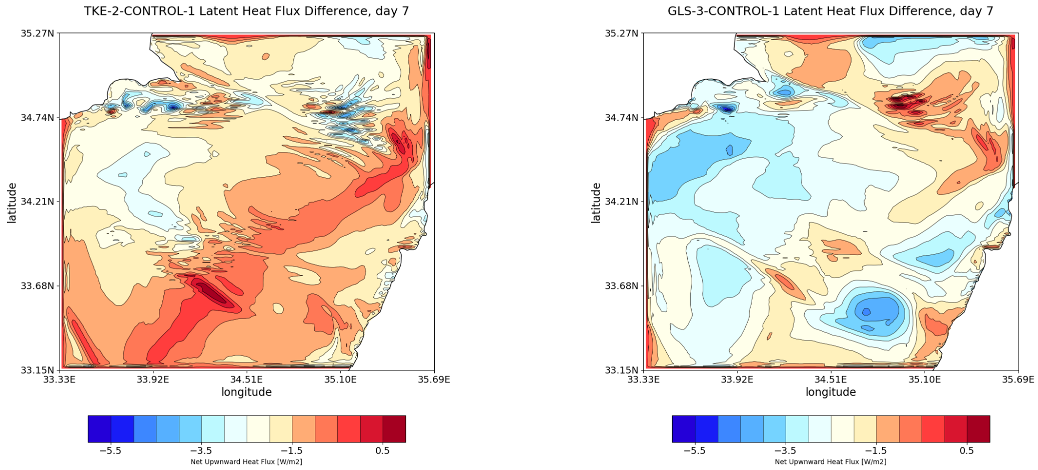

Figure 4.17: Latent Heat Flux difference, daily mean day 7/10/2020, between TKE-2 and Control (left panel) and between GLS-3 and Control (right panel).

The latent heat differences with Control, shown in Figure 4.17, shows that this component determines most of the overall difference in the total balance.
TKE-2 difference with the Control experiments shows values lower than -1 W/m^2 in most of the domain, with similar structures to TKE-1 case, with peaks about -3 W/m^2 in the negative values and about 1 W/m^2 in the positive values. This negative difference in the latent heat flux, corresponds to a minor evaporation flux and corresponds to a equal positive difference in the Net Heat Flux, having the latent component a negative sign in the Heat balance equation (as seen in equation 2.14).

GLS-3 difference with the Control experiments shows values inferior to -2 W/m^2 in most of the domain and inferior to -2.5 W/m^2 in about half of it, with similar structures to the previous comparison and peak values about -4 W/m^2 in the negative values and about 1 W/m^2 in the positive values. The same considerations about evaporation and Heat balance as done about TKE-2 are valid for GLS-3 with a decrease of the evaporation and an increase of the heat balance.

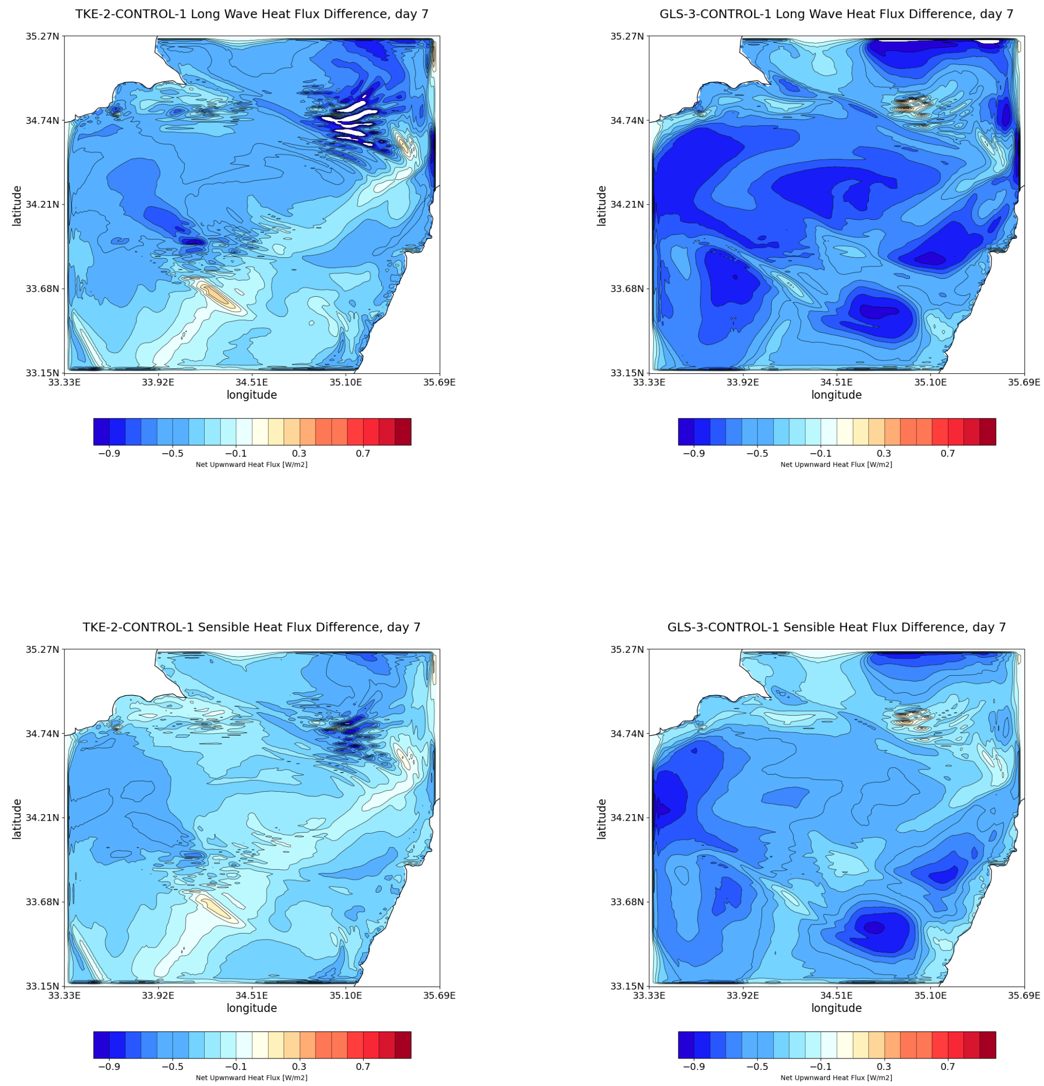

Figure 4.18: Top panels: Long Wave Heat Flux difference, daily mean day 7/10/2020, between TKE-2 and Control (left panel) and between GLS-3 and Control (right panel). Bottom panels: Sensible Heat Flux difference, daily mean day 7/10/2020, between TKE-2 and Control (left panel) and between GLS-3 and Control (right panel).

The Sensitive and Long Wave Heat Fluxes differences between the experiments and

Control show similar behaviours: in both of the comparisons both of the experiments show a negative trend, with limited values with respect to the Latent Heat Flux differences, but still significant in the total balance (about an order of magnitude lower). TKE shows differences under -0.4 W/m^2 in most of the domain with negative peaks of about the -0.9 W/m^2 and a positive peak of less than 0.3 W/m^2 in the Long Wave Heat difference. In the Sensible Heat flux differences had similar values with differences under -0.3 W/m^2 in most of the domain with negative peaks of about the -0.9 W/m^2 and a positive peak of less than 0.2 W/m^2 .

Since the Control Long Wave Heat flux had values around 90 W/m^2 these differences are relatively not very significant, meaning that this process was not affected by the change of parameterization; on the contrary the Control Sensible Heat values were rarely superior to 6 W/m^2, so even if not particularly relevant in the total balance the Sensible Heat Flux is significantly different between the two experiments.
GLS shows differences under -0.6 W/m^2 in most of the domain with negative peaks of about -0.9 W/m^2. In the Sensible Heat flux differences had similar values with differences under -0.4 W/m^2 in most of the domain with negative peaks of about the -0.9 W/m^2 and a positive peak of less than 0.2 W/m^2.

Again the Long Wave Heat flux difference are not very significant with respect to Control values, on the contrary the sensible heat flux relative differences are important reaching often values under -10 %.

Chapter 5

Conclusions

The goal of this thesis was the study of an optimal mixing parameterization scheme in a mesoscale dominated field characterized from a strong vorticity and the presence of a layer of colder, less saline water at about 100 m depth (Atlantic Waters); in these conditions we compared six different experiments, that differ by the turbulent closure schemes, the presence or not of an enhanced diffusion parameterization and the presence or not of a double diffusion mixing parameterization.
To evaluate the performance of the experiments and the model we compared the simulations with the ARGO observations of temperature and salinity available in our domain, in our period of interest.
The conclusions were the following:

- the increase of the resolution gives better results in terms of temperature in all the considered cases, and in terms of salinity.
- The comparisons between the Pacanovski-Philander and the TKE turbulent closure schemes don't show significant differences when the simulations are compared to the observations.
- The removing of the enhanced diffusion parameterization in presence of the TKE turbulent closure submodel doesn't give positive results, and show limitations in the resolving of gravitational instabilities near the surface
- The k-ϵ turbulent closure model utilized in all the GLS experiments, is the best performing closure model among the three considered, with positive results in all the salinity comparison with the in situ observation and in most of the temperature comparisons.
- The double mixing parameterization utilized in the k-ϵ closure submodel improves the results of the experiments improving both the temperature and salinity in comparison with the ARGO data.

- The removing of the enhanced diffusion parameterization in presence of the k-ϵ closure submodel further improves the results, improving both the temperature and salinity results in the comparison with the ARGO data.
- In the comparison between the GLS experiments with Control we noticed how these experiments are characterized from a better mixing in the upper layers with lower surface temperatures and salinity and a deeper mixed layer.
- The mixed layer depths of all the experiments are significantly lower in comparisons with the ARGO observations, this means that our experiments were not capable to simulate upward advection processes, probably due to a still missing horizontal resolution.

We can conclude that the optimal vertical mixing parameterization is a k-ϵ closure scheme with a double diffusion mixing parameterization, the modeling of the mixed layer to be further improved in order to provide adequate values of mixed layer depth.

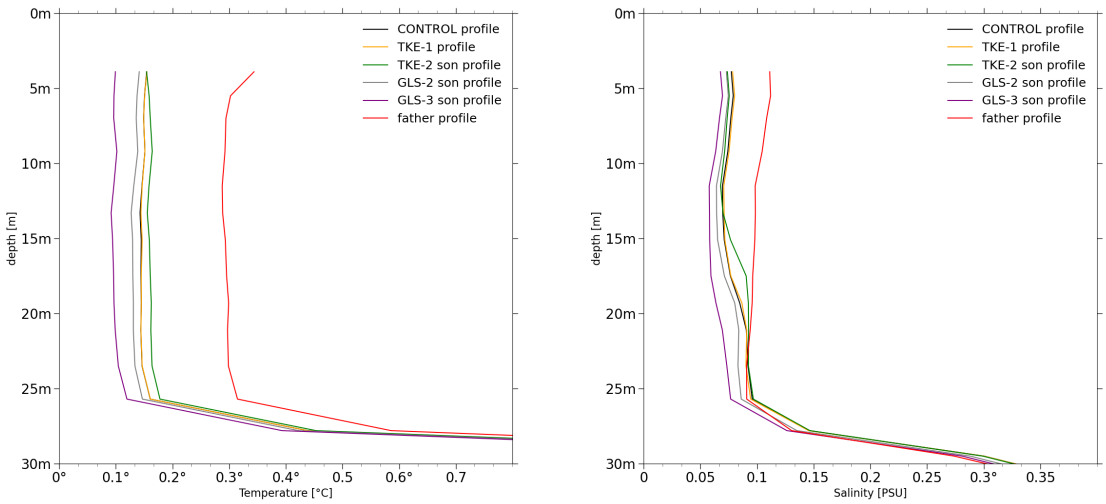

Figure 5.1: Root mean square error between the experiments and ARGO observations, Right Panel: salinity root mean square error between the experiments and the ARGO observations.
Left Panel: temperature root mean square error between the experiments and the ARGO observations.

In Fig. 5.1 we can see synthesized the behaviour of our experiments, with GLS-3 showing the minimum root mean square difference with respect to the ARGO observations in both mixed layer temperature and salinity profiles, also GLS-2 gives superior results with respect to the control experiment, with TKE-1 that is practically indistinguishable from Control, and TKE-2 that shows how in this case the removing of the enhanced diffusion had worsen the results.

Bibliography

Smith, N. R. (1993). Ocean modeling in a global ocean observing system. *Reviews of Geophysics*.

Talley, Pickard, Emery, & Swift. (2011). *Descriptive physical oceanography an introduction*.

Belcher, e. a. (2012). A global perspective on Langmuir turbulence in the ocean surface boundary layer. *Geophysical Research Letters*.

Pacanowski, & Philander. (1981). Parameterization of Vertical Mixing in Numerical Models of Tropical Oceans. *Journal of Physical Oceanography*.

Kantha, L. H., & Clayson, C. A. (1994). An improved mixed layer model for geophysical applications. *Journal of Geophysical Research*.

Mellor, & Blumberg. (2004). Wave breaking and ocean surface layer thermal response. *Journal of Physical Oceanography*.

Bougeault, P., & Lacarrere, P. (1989). Parameterization of Orography-Induced Turbulence in a Mesobeta–Scale Model. *Monthly Weather Review*.

Gaspar, P., Grégoris, Y., & Lefevre, J.-M. (1990). A simple eddy kinetic energy model for simulations of the oceanic vertical mixing: Tests at station Papa and long-term upper ocean study site. *Journal of Geophysical Research: Oceans*.

Blanke, B., & Delécluse, P. (1993). Variability of the Tropical Atlantic Ocean Simulated by a General Circulation Model with Two Different Mixed-Layer Physics. *Laboratoire d'océanographie dynamique et de climatologie*.

Madec, G., Delécluse, P., & Imbard, M. (1998). OPA 8.1 Ocean General Circulation Model reference manual. *Ocean Modelling*.

Ali, Christensen, & Breivik. (2019). A comparison of Langmuir turbulence parameterizations and key wave effects in a numerical model of the North Atlantic and Arctic Oceans. *Ocean Modelling*.

Gunduz, M., Dobricic, S., & Oddo, P. (2013). Impact of Levantine Intermediate Water on the interannual variability of the Adriatic Sea based on simulations with a fine resolution ocean model. *Ocean Modelling*.

Pinardi, & Masetti. (2000). Variability of the large scale general circulation of the Mediterranean Sea from observations and modelling: a review. *Palaeogeography, Palaeoclimatology, Palaeoecology*.

Pinardi, N., & Navarra, A. (1993). Baroclinic wind adjustment processes in the Mediterranean Sea. *Deep Sea Research Part II: Topical Studies in Oceanography.*

Wüst, G. (1961). On the vertical circulation of the Mediterranean Sea. *Journal of Geophysical Research.*

Nadia Pinardi, e. a. (2015). Mediterranean Sea large-scale low-frequency ocean variability and water mass formation rates from 1987 to 2007: A retrospective analysis. *Progress in Oceanography.*

Demirov, & Pinardi. (2007). On the relationship between the water mass pathways and eddy variability in the Western Mediterranean Sea. *Journal of Geophysical Research.*

Speich, Madec, & Crèpon. (1996). A strait outflow circulation process study: the case of the Alboran Sea. *Journal of Physical Oceanography.*

Gleizon, D'Hi´eres, C., & Renouard. (1996). Experimental study of the Alboran Sea gyres. *Oceanologica acta.*

Carter, D. B. (1956). *The water balance of the mediterranean and black seas.*

Lacombe, Tchernia, & Gamberoni. (1985). Variable bottom water in the Western Mediterranean basin. *Progress in Oceanography.*

Stommel, H. (1972). Circulation on the Continental Shelf. *Proceedings of the National Academy of Sciences of the United States of America.*

Larnicol, Ayoub, & Traon, L. (2002). Major changes in Mediterranean Sea level variability from 7 years of TOPEX/Poseidon and ERS-1/2 data. *Journal of Marine Systems.*

Poulain, Menna, & Mauri. (2012). Surface geostrophic circulation of the Mediterranean Sea derived from drifter and satellite altimeter data. *Journal of Physical Oceanography.*

Demirov, & Pinardi. (2002). Simulation of the Mediterranean Sea circulation from 1979 to 1993: Part i. The interannual variability. *Journal of Marine Systems.*

Molcard, Pinardi, & Iskandaranic. (2002). Wind driven general circulation of the Mediterranean Sea simulated with spectral element ocean model. *Dynamics of Atmospheres and Oceans.*

Fusco, Manzella, & Cruzado. (2003). Variability of mesoscale features in the Mediterranean Sea from XBT data analysis. *Annales Geophysicae.*

Leaman, & Schott. (2003). Hydrographic structure of the convective regime in the Gulf of Lions: Winter 1987. *Geophysical Reseach Oceanography.*

Artegiani, e. a. (1997). The Adriatic Sea general circulation. Part I: Air-sea interactions and water mass structure. *Journal of Physical Oceanography.*

Hecht, Pinardi, & Robinson. (1988). Currents, water masses, eddies and jets in the Mediterranean Levantine Basin. *Journal of Physical Oceanography.*

Tziperman, & Malanotte-Rizzoli. (1991). The climatological circulation of the Mediterranean Sea. *Journal of Marine Research.*

Ayoub, Traon, L., & Mey, D. (1998). A description of the Mediterranean surface variable circulation from combined ers-1 and topex/poseidon altimetric data. *Journal of Marine Systems.*

Korres, Pinardi, & Lascaratos. (2000). The ocean response to lowfrequency interannual atmospheric variability in the Mediterranean Sea. Part I: sensitivity experiments and energy analysis. *Journal of Climate.*

Astraldi, Bianchi, & Gasparini. (1995). Climatic fluctuations, current variability and marine species distribution: a case study in the Ligurian Sea (north-west Mediterranean). *Oceanologica Acta.*

Artale, Astraldi, & Buffoni. (1994). Seasonal variability of the gyre-scale circulation in the northern Tyrrhenian Sea. *Journal of Geophysical Research.*

Nittis, & Lascaratos. (1998). Diagnostic and prognostic numerical studies of LIW formation. *Journal of Marine Systems.*

Roether, & Manca, e. a. (1996). Recent changes in the Eastern Mediterranean Deep Waters. *Science.*

Hecht, A. (1992). Abrupt changes in the characteristics of Atlantic and Levantine intermediate waters in the Southeastern Levantine basin. *Oceanologica Acta.*

Trotta, F., Fenu, E., & Pinardi, N. (2016). A Structured and Unstructured grid Relocatable ocean platform for Forecasting (SURF). *Deep Sea Research Part II: Topical Studies in Oceanography.*

Trotta, F., Masina, S., & Pinardi, N. (2021). A Relocatable Ocean Modeling Platform for Downscaling to Shelf-Coastal Areas to Support Disaster Risk Reduction. *Frontiers in Marine Science.*

Oddo, & Pinardi. (2008). Lateral open boundary conditions for nested limited area models: A scale selective approach. *Ocean Modelling.*

Engedahl, H. (1995). Use of the flow relaxation scheme in a three-dimensional baroclinic ocean model with realistic topography. *Tellus A: Dynamic Meteorology and Oceanography.*

White, A. A., Hoskins, B. J., & Roulstone, I. (2005). Consistent approximate models of the global atmosphere: shallow, deep, hydrostatic, quasi-hydrostatic and non-hydrostatic. *Quarterly Journal of the Royal Meteorological Society.*

Gent, P., & Mcwilliams, J. (1990). Isopycnal Mixing in Ocean Circulation Models. *Journal of Physical Oceanography.*

Kolmogorov, A. N. (1941). The Local Structure of Turbulence in Incompressible Viscous Fluid for Very Large Reynolds Number. *Proceedings: Mathematical and Physical Sciences.*

Craig, & Banner. (1994). Modeling wave-enhanced turbulence in the ocean surface layer. *Journal of Physical Oceanography.*

Stacey, M. W. (1999). Simulations of the wind-forced near-surface circulation in Knight Inlet: A parameterization of the roughness length. *Journal of Physical Oceanography.*

Axell, L. B. (2002). Wind-driven internal waves and Langmuir circulations in a numerical ocean model of the southern Baltic Sea. *Journal of Geophysical Research.*

D'Alessio, Abdella, & McFarlane. (1998). A new second-order turbulence closure scheme for modeling the oceanic mixed layer. *Journal of Physical Oceanography.*

Galperin, Kantha, & Rosati, A. (1988). A quasi-equilibrium turbulent energy model for geophysical flows. *Journal of the Atmospheric Sciences.*

Merryfield, W. J., Holloway, G., & Gargett, A. E. (1999). A Global Ocean Model with Double-Diffusive Mixing. *Journal of Physical Oceanography.*

Schmitt, R. W. (1981). Form of the Temperature-Salinity Relationship in the Central Water, Evidence for Double-Diffusive Mixing. *Journal of Physical Oceanography.*

Federov, K. N. (1988). Layer thicknesses and effective diffusivities in "diffusive" thermohaline convection in the ocean. *Small-Scale Turbulence and Mixing in the Ocean.*

Lazar, A. (1997). La branche froide de la circulation thermohaline - sensibilité à la diffusion turbulente dans un modèle de circulation générale idéalisée. *Ph.D. thesis, Université Pierre et Marie Curie.*

Pinardi, N., Allen, I., & Demirov, E. (2003). The Mediterranean ocean forecasting system: first phase of implementation (1998–2001). *Annales Geophysicae.*

Pinardi, & Coppini. (2010). Operational oceanography in the Mediterranean Sea: the second stage of development. *Ocean Science.*

Tonani, M., Teruzzi, A., & Korres, G. (2014). The Mediterranean Monitoring and Forecasting Centre, a component of the MyOcean system. *Proceedings of the 6th Int. Conference on EuroGOOS 4-6 October 2011.*

Clementi, E., Pistoia, J., & Delrosso, D. (2017). A 1/24 degree resolution Mediterranean analysis and forecast modelling system for the Copernicus Marine Environment Monitoring Service. *Extended abstract to the 8th EuroGOOS Conference, Bergen.*

Leer, B. V. (1979). Towards the ultimate conservative difference scheme. V. A second-order sequel to Godunov's method. *Journal of Computational Physics.*

Oddo, Adani, & Pinardi. (2009). A Nested Atlantic Mediterranean Sea General Circulation Model for Operational Forecasting. *Ocean Science.*

Pettenuzzo, Large, & Pinardi. (2010). On the corrections of ERA-40 surface flux products consistent with the Mediterranean heat and water budgets and the connection between basin surface total heat flux and NAO. *Journal of Geophysical Research.*

Oddo, Bonaduce, & Pinardi. (2014). Sensitivity of the Mediterranean sea level to atmospheric pressure and free surface elevation numerical formulation in NEMO. *Geoscientific Model Development.*

Maderich, V., Ilyin, Y., & Lemeshko, E. (2015). Seasonal and interannual variability of the water exchange in the Turkish Straits System estimated by modelling. *Mediterranean Marine Science.*

Srdjan, D., & Pinardi, N. (2008). An oceanographic three-dimensional variational data assimilation scheme. *Ocean Modelling.*

Storto, A., Masina, S., & Navarra, A. (2015). Evaluation of the CMCC eddy-permitting global ocean physical reanalysis system (C-GLORS, 1982-2012) and its assimilation components. . *Quarterly Journal of the Royal Meteorological Society.*

Trotta, F., Pinardi, N., & Fenu, E. (2017). Multi-nest high-resolution model of submesoscale circulation features in the Gulf of Taranto. *Ocean Dynamics.*

Marullo, S., Santoleri, R., & Ciani, D. (2014). Combining model and geostationary satellite data to reconstruct hourly SST field over the Mediterranean Sea. *Remote Sensing of Environment.*

Ozsoy, Latif, & Unluata. (1981). On the formation of Levantine intermediate water. *Rapports et Proces-Verbaux des Reunions - Commission Internationale pour l'Exploration Scientifique de la Mer Mediterranee.*

Griffies, S., Böning, C. W., & Bryan, F. O. (2000). Developments in Ocean Climate Modelling. *Ocean Modelling.*

Rodi, W. (1987). Examples of calculation methods for flow and mixing in stratified fluids. *Journal of Geophysical Research.*